The Astrophysical Journal, 974:239 (20pp), 2024 October 20 https://doi.org/10.3847/1538-4357/ad6a5f

JCMT 850 μm Continuum Observations of Density Structures in the G35 Molecular Complex

Xianjin Shen[1,35], Hong-Li Liu[1,35], Zhiyuan Ren[2,3,4], Anandmayee Tej[5], Di Li[2,6,7], Hauyu Baobab Liu[8,9], Gary A. Fuller[10,11], Jinjin Xie[2], Sihan Jiao[3,4], Aiyuan Yang[2,12,13], Patrick M. Koch[14], Fengwei Xu[15,16], Patricio Sanhueza[17,18], Pham Ngoc Diep[19], Nicolas Peretto[20], R. K. Yadav[21], Busaba H. Kramer[13,21], Koichiro Sugiyama[21], Mark G. Rawlings[22], Chang Won Lee[23,24], Ken'ichi Tatematsu[17,18], Daniel Harsono[25], David Eden[26], Woojin Kwon[27,28], Chao-Wei Tsai[2,4,29], Glenn J. White[30,31], Kee-Tae Kim[24,23], Tie Liu[32], Ke Wang[15], Siju Zhang[15], Wenyu Jiao[15,16], Dongting Yang[1], Swagat R. Das[33,34], Jingwen Wu[2,4], and Chen Wang[2]

[1] School of Physics and Astronomy, Yunnan University, Kunming, 650091, People's Republic of China; hongliliu2012@gmail.com
[2] National Astronomical Observatories, Chinese Academy of Sciences, Datun Road A20, Beijing, People's Republic of China; jeremyrzy@gmail.com
[3] CAS Key Laboratory of FAST, NAOC, Chinese Academy of Sciences, Beijing, People's Republic of China
[4] University of Chinese Academy of Sciences, Beijing, People's Republic of China
[5] Indian Institute of Space Science and Technology, Thiruvananthapuram, Kerala 695 547, India; tej@iist.ac.in
[6] Department of Astronomy, Tsinghua University, Beijing 100084, People's Republic of China
[7] Zhejiang Lab, Hangzhou, Zhejiang 311121, People's Republic of China
[8] Department of Physics, National Sun Yat-Sen University, No. 70, Lien-Hai Road, Kaohsiung City 80424, Taiwan
[9] Center of Astronomy and Gravitation, National Taiwan Normal University, Taipei 116, Taiwan
[10] Jodrell Bank Centre for Astrophysics, School of Physics and Astronomy, University of Manchester, Oxford Road, Manchester M13 9PL, UK
[11] Physikalisches Institut, University of Cologne, Zülpicher Str. 77, D-50937 Köln, Germany
[12] Key Laboratory of Radio Astronomy and Technology, Chinese Academy of Sciences, A20 Datun Road, Datun Road A20, Beijing, People's Republic of China
[13] Max-Plank-Institut für Radioastronomie, Auf dem Hügel 69, D-53121 Bonn, Germany
[14] Academia Sinica Institute of Astronomy and Astrophysics, No. 1, Sec. 4, Roosevelt Road, Taipei 10617, Taiwan
[15] Kavli Institute for Astronomy and Astrophysics, Peking University, 5 Yiheyuan Road, Haidian District, Beijing 100871, People's Republic of China
[16] Department of Astronomy, School of Physics, Peking University, Beijing 100871, People's Republic of China
[17] National Astronomical Observatory of Japan, National Institutes of Natural Sciences, 2-21-1 Osawa, Mitaka, Tokyo 181-8588, Japan
[18] Astronomical Science Program, The Graduate University for Advanced Studies, SOKENDAI, 2-21-1 Osawa, Mitaka, Tokyo 181-8588, Japan
[19] Vietnam National Space Center, Vietnam Academy of Science and Technology, 18 Hoang Quoc Viet, Hanoi, Vietnam
[20] Cardiff Hub for Astrophysics Research & Technology, School of Physics & Astronomy, Cardiff University, Queens Buildings, The Parade, Cardiff CF24 3AA, UK
[21] National Astronomical Research Institute of Thailand (NARIT), Sirindhorn AstroPark, 260 Moo 4, T. Donkaew, A. Maerim, Chiangmai 50180, Thailand
[22] Gemini Observatory/NSF's NOIRLab, 670 N. A'ohōkū Place, Hilo, HI 96720, USA
[23] Korea Astronomy and Space Science Institute, 776 Daedeokdae-ro, Yuseong-gu, Daejeon 34055, Republic of Korea
[24] University of Science and Technology, Korea (UST), 217 Gajeong-ro, Yuseong-gu, Daejeon 34113, Republic of Korea
[25] Institute of Astronomy, Department of Physics, National Tsing Hua University, Hsinchu 30013, Taiwan
[26] Armagh Observatory and Planetarium, College Hill, Armagh BT61 9DB, UK
[27] Department of Earth Science Education, Seoul National University, 1 Gwanak-ro, Gwanak-gu, Seoul 08826, Republic of Korea
[28] SNU Astronomy Research Center, Seoul National University, 1 Gwanak-ro, Gwanak-gu, Seoul 08826, Republic of Korea
[29] Institute for Frontiers in Astronomy and Astrophysics, Beijing Normal University, Beijing 102206, People's Republic of China
[30] School of Physical Sciences, The Open University, Walton Hall, Milton Keynes MK7 6AA, UK
[31] RAL Space, STFC Rutherford Appleton Laboratory, Chilton, Didcot, Oxfordshire OX11 0QX, UK
[32] Shanghai Astronomical Observatory, Chinese Academy of Sciences, 80 Nandan Road, Shanghai 200030, People's Republic of China
[33] Departamento de Astronomia, Universidad de Chile, Las Condes, 7591245 Santiago, Chile
[34] Indian Institute of Science Education and Research (IISER) Tirupati, Rami Reddy Nagar, Karakambadi Road, Mangalam (P.O.), Tirupati 517507, India
Received 2024 March 12; revised 2024 July 28; accepted 2024 July 29; published 2024 October 15

Abstract

Filaments are believed to play a key role in high-mass star formation. We present a systematic study of the filaments and their hosting clumps in the G35 molecular complex using James Clerk Maxwell Telescope SCUBA-2 850 μm continuum data. We identified five clouds in the complex and 91 filaments within them, some of which form 10 hub–filament systems (HFSs), each with at least three hub-composing filaments. We also compiled a catalog of 350 dense clumps, 183 of which are associated with the filaments. We investigated the physical properties of the filaments and clumps, such as mass, density, and size, and their relation to star formation. We find that the global mass–length trend of the filaments is consistent with a turbulent origin, while the hub-composing filaments of high line masses ($m_l > 230\,M_\odot\,\mathrm{pc}^{-1}$) in HFSs deviate from this relation, possibly due to feedback from massive star formation. We also find that the most massive and densest clumps ($R > 0.2$ pc, $M > 35\,M_\odot$, $\Sigma > 0.05\,\mathrm{g\,cm}^{-2}$) are located in the filaments and in the hubs of HFSs, with the latter bearing a higher probability of the occurrence of high-mass star-forming signatures, highlighting the preferential

[35] Both authors contributed equally to this work.

sites of HFSs for high-mass star formation. We do not find significant variation in the clump mass surface density across different evolutionary environments of the clouds, which may reflect the balance between mass accretion and stellar feedback.

Unified Astronomy Thesaurus concepts: Star formation (1569); Star forming regions (1565); Molecular clouds (1072); Interstellar filaments (842); Molecular gas (1073); Dust continuum emission (412)

Materials only available in the online version of record: machine-readable tables

1. Introduction

High-mass stars ($M > 8\,M_{\odot}$) significantly contribute to the energy and momentum of galaxies through their radiation, stellar winds, massive outflows, expanding H II regions, and supernova explosions (Zinnecker & Yorke 2007; Motte et al. 2018). Despite their importance, the formation process of these stars remains less understood than that of their low-mass counterparts, primarily due to their short lifetimes, great distances, intense accretion processes, and significant feedback effects.

Observational studies have revealed the ubiquity of filamentary structures in the Milky Way (e.g., André et al. 2010; Molinari et al. 2010; Kumar et al. 2020; Schisano et al. 2020; Zavagno et al. 2023 and references therein). These studies have also highlighted a strong correlation between star formation and filamentary molecular clouds (e.g., André et al. 2014; Lu et al. 2014, 2018; Liu et al. 2020, 2022). Intersecting filaments create distinct web structures, known as hub–filament systems (HFSs), representing a unique class of filaments in star formation, particularly for high-mass stars (e.g., Myers 2009; H. B. Liu et al. 2012b; Wang et al. 2016; Kumar et al. 2020; Zhou et al. 2022; H.-L. Liu et al. 2023). In the context of HFSs, the central node is referred to as the hub, while the individual filaments associated with it are termed hub-composing filaments.

Recent studies of HFSs (e.g., H. B. Liu et al. 2012a; Peretto et al. 2013, 2014; Yuan et al. 2018; H.-L. Liu et al. 2019; Ren et al. 2021; Sanhueza et al. 2021; Saha et al. 2022; Yang et al. 2023b; He et al. 2023; Xu et al. 2023; Pan et al. 2024) have invoked the latest high-mass star formation models, such as global hierarchical collapse (GHC, Vázquez-Semadeni et al. 2019) and inertial inflow (I2, Padoan et al. 2020) to understand star formation in these systems. In such models, filamentary structures are predicted to undergo self-growth through radial accretion from their surrounding environment and to supply the formed clumps or cores through longitudinal accretion. Therefore, investigating how the physical proprieties (e.g., mass, density, size) of these hierarchical density structures evolve with time is helpful to understanding the complete picture of star formation, especially high-mass star formation. To this end, conducting observational studies of large samples of filaments and embedded dense structures at different stages of evolution becomes the focus of this study.

The structure of the paper is as follows: Sections 2 and 3 describe the targeted region and the observations, respectively. Section 4 presents the results and analysis, focusing on distance measurement, identification of structures, and derivation of relevant physical parameters. Section 5 discusses the star formation scenario in the complex investigated. Specifically, Section 5.1 delves into the fragmentation of filaments; Section 5.2 discusses the role of HFS clouds in massive star formation; Section 5.3 explores the evolution of clump density over time. Section 6 gives the summary and conclusions.

2. Presentation of the Targeted Region

The G35 molecular complex is selected as the target region investigated here due to the presence of many filamentary structures at different evolutionary stages. The target region, centered at $\alpha_{2000} = 18^{\rm h}56^{\rm m}28^{\rm s}.16$, $\delta_{2000} = 2^{\circ}14'25.''71$ ($l = 35.^{\circ}499$, $b = -0.^{\circ}097$), with an approximate radius of $0.^{\circ}41$, covers five individual clouds, which correspond to different systemic velocities (see Section 4.1) and thus are designated as Clouds 1, 2, 3, 4, and 5 (see Figure 1).

Cloud 1, Cloud 2, and Cloud 3 harbor infrared dark clouds (IRDCs). Six IRDCs (i.e., G35.39, G35.60, and G35.69 in Cloud 1, G35.41 and G35.54 in Cloud 2, and G35.46 in Cloud 3), as candidate sites for high-mass star formation, were cataloged by Peretto & Fuller (2009). One of them, G35.39, located at ∼2.9 kpc (Simon et al. 2006), is a well-known star-forming ridge (Nguyen Luong et al. 2011; Motte et al. 2018) that has been extensively studied for its fragmentation, kinematics, dust polarization, and/or chemical properties (e.g., Sanhueza et al. 2012; Jiménez-Serra et al. 2014; Barnes et al. 2016, 2021; Sokolov et al. 2017; Liu et al. 2018; Xie et al. 2021). In comparison, IRDC G35.41, exhibiting a bipolar bubble feature in the 8 μm image, is at a more evolved stage. The elongated IRDC G35.46 in Cloud 3, together with IRDC G35.41 and G35.54 in Cloud 2, and IRDC G35.60 and G35.69 in Cloud 1, are less well studied. In addition, the entire targeted region contains 37 ATLASGAL clumps (Urquhart et al. 2014a, 2018), about a quarter of which are located within the IRDCs.

The other molecular cloud complex in the northern region is Cloud 4, centered at $\alpha_{2000} = 18^{\rm h}56^{\rm m}09^{\rm s}.55$, $\delta_{2000} = 2^{\circ}22'58.''99$. This cloud, approximately $0.^{\circ}2$ in radius (corresponding to a physical scale of ∼10 pc), exhibits extended morphology and is bright in the IR. Its eastern side is connected to a large IR bubble (i.e., G356521-0002439; Jayasinghe et al. 2019), denoted as the largest magenta circle. The entire cloud encompasses several smaller IR bubbles surrounding H II regions (Anderson et al. 2014), also marked with colored circles in Figure 1. Three massive young stellar objects (MYSOs) and a Wide-field Infrared Survey Explorer (WISE) Green Object (WGO) G35.417-0.285 denoted in Figure 1 can be found within Cloud 4 (Urquhart et al. 2008; Zhang et al. 2023). Furthermore, the Spitzer/IRAC candidate young stellar object (YSO) catalog for the inner Galactic midplane project (SPICY; Kuhn et al. 2021) has revealed a group of over 300 young YSO candidates, which are not shown here. Fourteen H II regions and six methanol masers at 6.7 GHz, both suggestive of high-mass star formation, have been observed in this large area containing the four primary clouds by the Global View on Star Formation (GLOSTAR) survey with high-resolution Very Large Array observations (Brunthaler et al. 2021; Nguyen et al. 2022; Yang et al. 2023a; Dzib et al. 2023).

Cloud 5 appears to harbor four bubbles identified as (candidate) H II regions (Anderson et al. 2014), one of which is associated with a methanol maser at 6.7 GHz. In this cloud

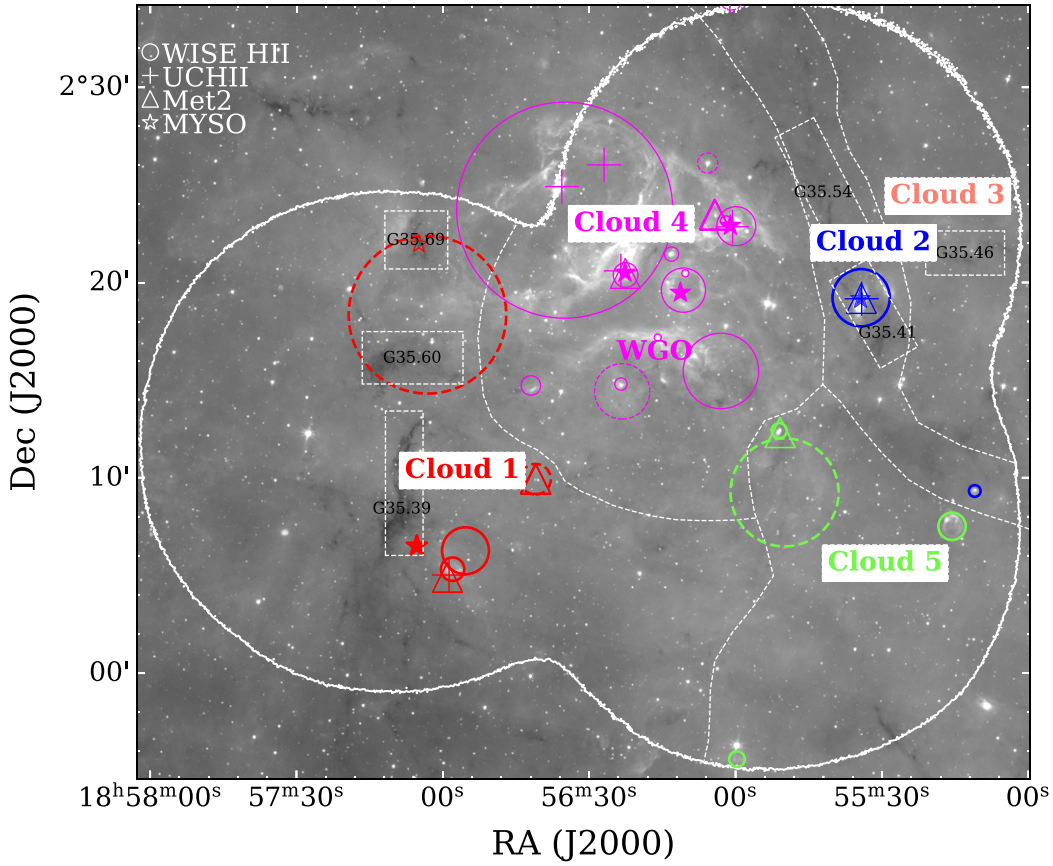

Figure 1. Overview of the G35 complex in Spitzer 8 μm emission. The solid and dashed circles correspond to the H II regions and candidates from the WISE catalog by Anderson et al. (2014), respectively, with the symbol size representing the actual size of those objects. The plus symbols identify the positions of ultracompact H II regions from different literature catalogs (Bronfman et al. 1996; Hou & Han 2014; Hu et al. 2016; Kalcheva et al. 2018; Ouyang et al. 2019). The class II methanol masers retrieved from Ladeyschikov et al. (2019) and Nguyen et al. (2022) are marked by open triangles. The solid stars identify the red Midcourse Space Experiment MYSOs (Urquhart et al. 2011) while the open stars identify massive protostars (Li et al. 2018). Six dark clouds mentioned in Section 2 with their names are marked using white dashed rectangles. The white dashed lines approximately delineate boundaries of different clouds. The region of 850 μm continuum for final analysis is limited within a white solid contour of the 20 mJy beam^{-1} rms level.

along with Cloud 3, most of the region shows relatively weak cold dust emission as traced by 850 μm radiation (see Section 4.2 and Figure 2), which is similar to the low intensity contrast observed in 8 μm emission.

In summary, the entire target complex encompasses active high-mass star-forming clouds at various evolutionary phases, from quiescent IRDCs to evolved bubbles or H II regions.

3. Observations

3.1. SCUBA-2 850 μm Continuum Data

The G35 molecular complex was observed as part of the 850 μm dust continuum survey, called "A Lei of the Habitat and Assembly of Infrared Dark Clouds" (ALOHA IRDCs[36]) under a James Clerk Maxwell Telescope (JCMT) large program (Proj. ID M20AL021; Z.-Y. Ren et al. 2024, in preparation). The survey was performed using the SCUBA-2 rotating Pong900 pattern. The entire observing coverage of the target region, which is delineated as the outermost white contour in Figure 1, consists of three fields of view (FOV), each observed with a radius of approximately 15′ at a scan spacing of 30″. The entire target was observed with an integration time of 22 hr. Raw data were reduced using the *Starlink*[37] software, yielding a final reduced 850 μm image and an rms noise map. The noise level varies between 5 and 75 mJy beam^{-1} from the inner region to the edge, and the global rms distribution appears, except for the regions approaching the edge, reasonably uniform at an approximate 10 mJy beam^{-1} (see Figure A1). The beam size of the reduced data is 14.″1 and the adopted pixel size for mapping is 4″. The flux calibration uncertainty of SCUBA-2 at 850 μm is $\sim$6% (Mairs et al. 2021). Note that ground-based (sub)millimeter continuum observations usually suffer from missing flux at large scales (e.g., Jiao et al. 2022) in the data-processing stage, since a filter has to be applied to remove large-scale atmospheric noises. Following the SCUBA-2 Data Reduction Cookbook,[38] a default filter scale of 480″ was adopted. This translates to scales >4.5 pc at the distance of the G35 complex and thus is assumed not to significantly affect the smaller-scale dense structures of filaments (i.e., ~0.5 pc in typical width) and clumps investigated here (see also Schuller et al. 2009; Li et al. 2016; Urquhart et al. 2018).

[36] https://www.eaobservatory.org/jcmt/science/large-programs/aloha-irdcs/

[37] https://starlink.eao.hawaii.edu/starlink

[38] http://starlink.eao.hawaii.edu/devdocs/sc21.htx/sc21.html

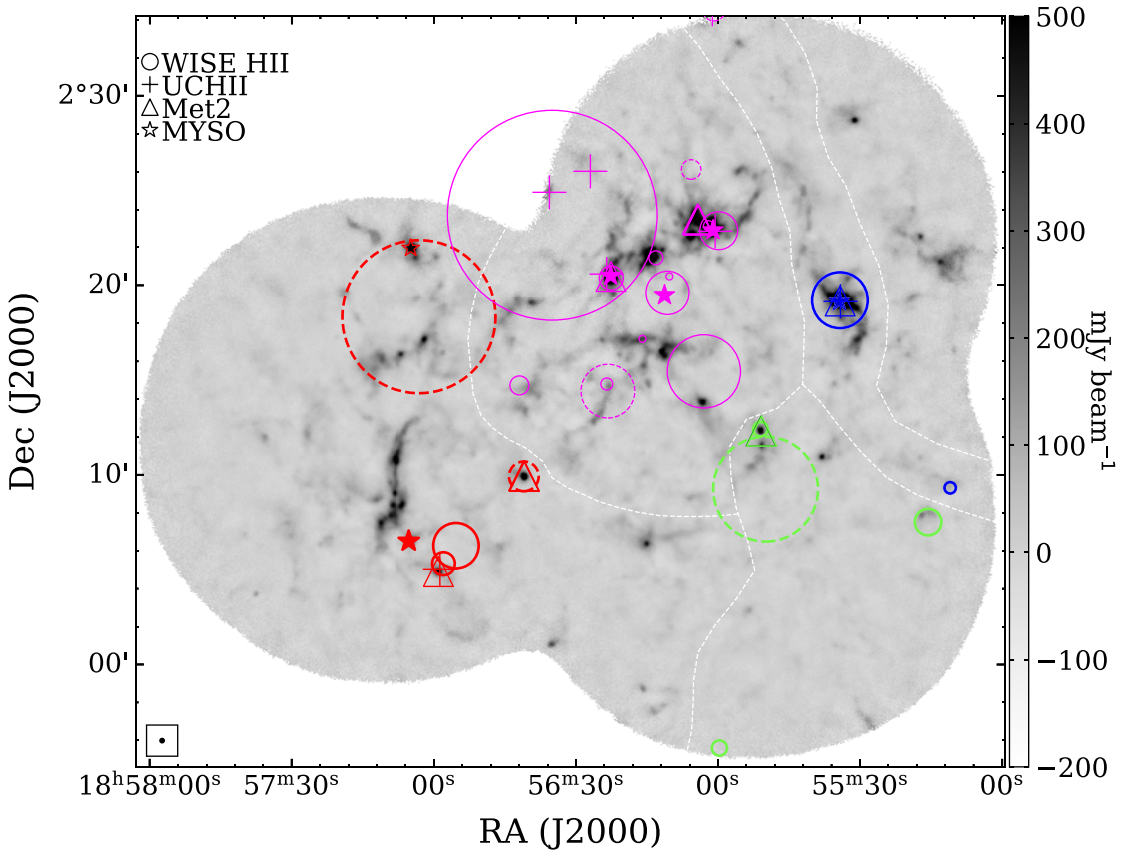

Figure 2. Dust emission maps as traced by 850 μm continuum for the G35 complex. All symbols are the same as those in Figure 1. The beam size of 850 μm observations is displayed at the bottom left corner.

3.2. Archival Data

We used multiwavelength infrared images from the Spitzer and Herschel telescopes to study the dust properties of the cloud complex. These include Spitzer 8 μm data from the GLIMPSE (Benjamin et al. 2003) survey and Herschel data (160 μm and 250 μm) from the Hi-GAL survey (Molinari et al. 2010). The angular resolutions at 8 μm, 160 μm, and 250 μm are approximately 2″, 12″, and 18″, respectively.

Molecular line observations of ^{13}CO ($J = 1$–0) were obtained as part of the Boston University–Five College Radio Astronomy Observatory Galactic Ring Survey (GRS; Jackson et al. 2006) using the FCRAO 14 m telescope. The data have an rms sensitivity $<$0.4 K, a spectral resolution of 0.21 km s^{-1}, and an angular resolution of 46″.

4. Results

4.1. Distance Determination

Except for the well-studied IRDC G35.39-0.33 located at 2.9 kpc (Simon et al. 2006; Liu et al. 2018), the distances for the remaining clouds in the region targeted here have not yet been determined. Figure A2 in Appendix A displays the average spectra of ^{13}CO over the entire target region. Five strong velocity components are seen in the ^{13}CO line with velocity ranges [5, 20], [20, 40], [40, 50], [50, 65], and [70, 85] km s^{-1}. With the assumption that cold dust emission comes from the the same region as molecular gas, the velocity-integrated intensity of ^{13}CO of these velocity components can be used to investigate their spatial association with the 850 μm dust continuum. Based on this, we exclude the second velocity component from further analysis. That component is most likely not associated, as the line and dust emission do not spatially match well. The integrated intensity of ^{13}CO of four velocity components is presented in Figure A3, showing a good association between gas and dust emission, excluding the second component. Note that there are overlapping distributions of relatively weak gas emission from different velocity components, such as the overlap between Cloud 5 and Cloud 2 (Figure A3). This indicates that the observed dust emission is likely contaminated by the line-of-sight contamination of clouds at different distances.

Based on the above-mentioned spatial association in 850 μm dust continuum emission, five primary clouds shown in Figure 1 have been approximately delineated. The separation between Cloud 1 and Cloud 4 is roughly based on the appearance of relatively dark and bright 8 μm features, and hence is to be considered with caution and for guidance only. The associated four velocity components are considered to derive kinematic distances using the latest distance calculation tool, the "Parallax-Based Distance Calculator V2" (Reid et al. 2016, 2019), leading to distance estimates of 2.1 kpc (i.e., Cloud 5), 2.5 kpc (i.e., Cloud 1, Cloud 3, and Cloud 4), and 5.1 kpc (i.e., Cloud 2), all with an uncertainty of $\sim$10%. The distance estimates of Clouds 1, 3, and 4 are very close to that of IRDC 035.39-0.33. Therefore, they are assumed to be in the same complex, and are treated for consistency as having the same distance as that of the well-studied IRDC G35.39 (i.e., 2.9 kpc).

4.2. Dust Continuum Emission

Figure 2 shows the 850 μm dust emission image. As an excellent tracer of column density, the continuum peak emission matches the 8 μm dark lanes. Overall, Clouds 1, 2, and 4 account for the vast majority of the continuum emission, while the continuum emission from Clouds 3 and 5 is relatively weak.

4.3. Identification of Filaments and Clumps

4.3.1. Filament Extraction

Filamentary structures were extracted from the 850 μm continuum image using the algorithm `FILFINDER` (Koch & Rosolowsky 2015). We set the minimum threshold (`glob_thresh`) to five times the rms ($\sim$50 mJy beam^{-1}), the minimum structure area (`size_thresh`) to 18 pixels (twice the beam area), and the hole-filling size (`fill_hole_size`) to 150 pixels. Here, the first two parameters were determined to improve the robustness of the identified skeletons, while the third one was to avoid the presence of holes within a skeleton. During our post-selection, we discarded structures at the image edges and those in the areas with rms greater than 20 mJy beam^{-1}. We also removed structures with a major axis (length) shorter than three beam sizes, following Suri et al. (2019). As a result, we obtained 91 skeletons representing individual filaments, some of which form HFSs (see Section 1 for their definition).

The identified filaments are shown in Figures 4 and A4. Overall, Cloud 1 is found to contain 17 individual filaments and three HFSs (i.e., each HFS corresponding to a web of at least three individual filaments[39]). Cloud 2 has seven individual filaments and two HFSs. Cloud 3 hosts four individual filaments and one HFS. Cloud 4 consists of 15 individual filaments and four HFSs. Cloud 5 shows three individual filaments. Note that there could be a few filaments that were not identified due to the strict criteria we adopted (e.g., 5 rms as the minimum threshold) for a robustness. This incompleteness caused by a few unidentified filaments, however, does not affect our following analysis. In addition, we find that all HFSs identified here are included in the catalog of filaments by Li et al. (2016) using ATLASGAL 870 μm dust emission observed at a similar angular resolution but with a lower sensitivity (i.e., 50–70 mJy beam^{-1}). In all, except for more detection of fainter structures in our observations, the dense filament detection has a good correspondence between the two different observations.

4.3.2. Clump Extraction

We created the clump catalog using the source extraction algorithm `SExtractor` (Bertin & Arnouts 1996), an aperture photometry tool widely used to detect compact objects (e.g., Contreras et al. 2013; Urquhart et al. 2014a). The 850 μm map and the noise rms map serve as input to `SExtractor`, with a detection threshold of five times the local rms. The total flux of each object is measured from the 850 μm map adopting the "Bijection" paradigm (see Figure 4 of Rosolowsky et al. 2008) using ellipse aperture photometry. The final uncertainty in the measured flux arises from the combination in quadrature of the local noise with the systematic flux uncertainty (e.g., Thompson et al. 2006; Contreras et al. 2013). As a result, 350 compact density structures are extracted, which are hereafter called clumps. Note that a few clumps appear not be extracted, for example in the northernmost part of the observing region, which could be either due to the low intensity contrast (i.e., $<5\times$ the signal-to-noise ratio, S/N) with the local rms level or due to their sizes being smaller than the beam size accessible to 850 μm observations. The latter possibility could be due to potential artifacts of the continuum map, and thus those associated sources are not considered in our analysis of the clump catalog.

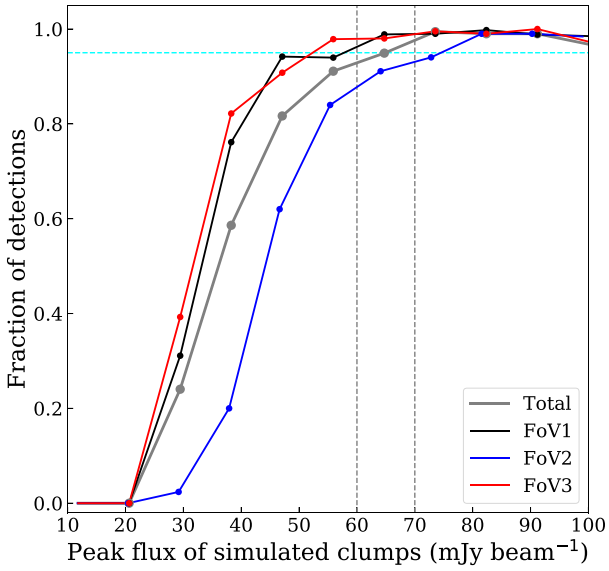

Figure 3. Detection fraction of simulated sources as a function of peak flux density. Different curves correspond to different FOV analysis, for FOVs 1, 2, and 3 and their sum as the total FOV. The dashed cyan line indicates the 95% detection fraction/flux completeness level. Two dashed gray lines (from left to right) show the 6 rms and 7 rms levels (1 rms = 10 mJy beam^{-1}).

It is necessary to investigate the flux completeness level of our cataloged clumps given the limitation of the observing sensitivity. To this end, we randomly inserted simulated clumps into the 850 μm noise map (e.g., Contreras et al. 2013; Yang et al. 2023a). We simulated 5000 clumps for each FOV analysis, with the input flux densities ranging from 1 to 100 mJy beam^{-1} (for reference, 1 rms = 10 mJy beam^{-1} overall). Here, three individual FOVs (see Figure A1), each representing different observations, and their sum as the entire FOV were considered, each having slightly different rms distributions. Subsequently, the same Sextractor algorithm was applied to the simulated map. Figure 3 illustrates the detection fraction of the simulated clumps as a function of peak flux density. As a result, the 95% completeness levels are $\sim$6 rms for FOVs 1 and 3, $\sim$7 rms for FOV 2, and approximately $\sim$6.5 rms ($N_{H_2} \approx 4.3 \times 10^{21}$ cm^{-2}) for the entire FOV. This suggests that the slight difference in different FOVs does not significantly affect the detection of clumps. In addition, the 5 rms level adopted in practice in our clump extraction corresponds to a global flux completeness level of $\sim$90% for the entire FOV.

The measured parameters of the 350 clumps identified are listed in Table B2, including the position, peak flux, and position angle. Figure 4 shows the identified clumps overlaid on the 850 μm continuum. The majority of the detected clumps

[39] By definition, the HFS structure is required to have at least three hub-composing filaments. This would allow us to rule out the possibility of a single filament appearing as an HFS structure due to the kink by external pressures instead of the merger process by several filaments.

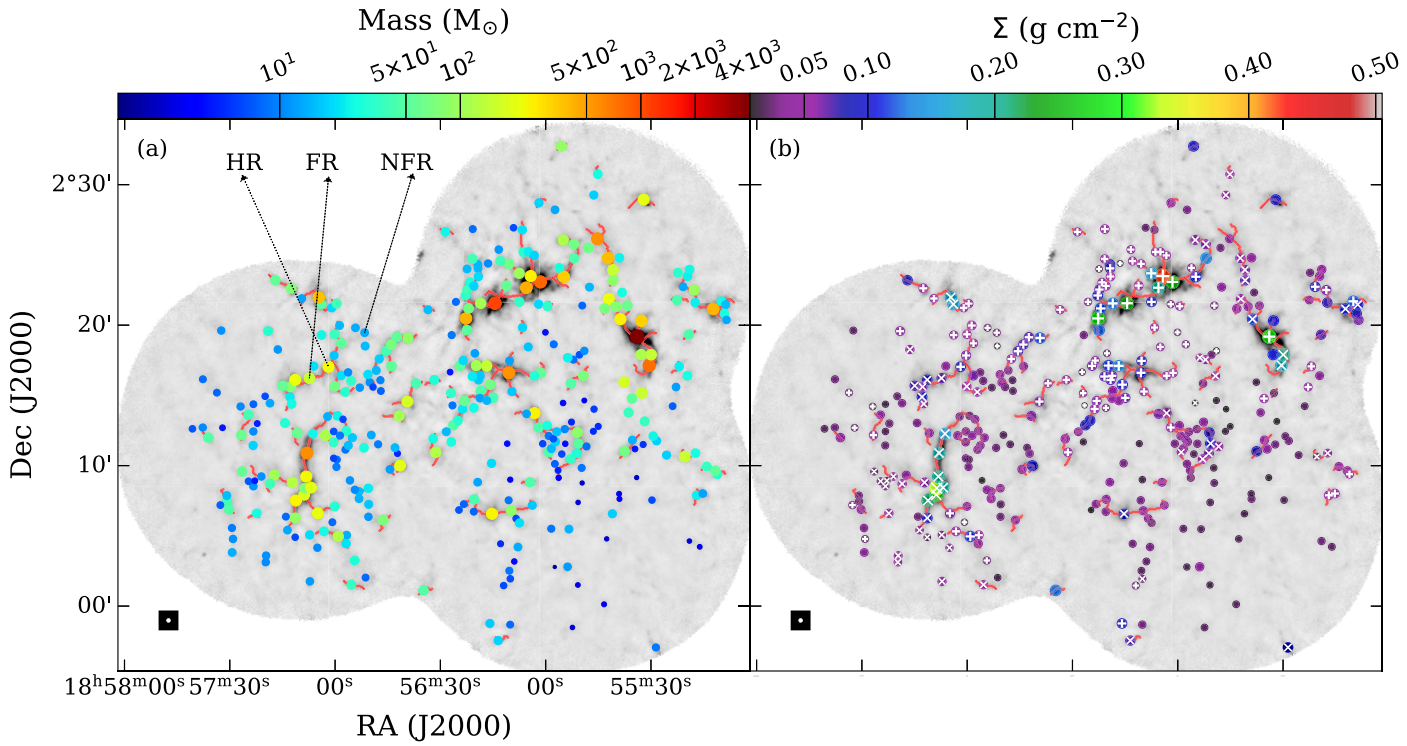

Figure 4. Spatial distributions of filaments (red curves) and clumps (colored dots). In (a) the color of the dot corresponds to the value of the clump mass, while in (b) it corresponds to the value of the mass surface density. In both panels, the white plus and cross symbols indicate IR-bright and IR-dark clumps inferred from Spitzer 8 μm images, respectively. The examples of HR clumps, FR clumps, and NFR clumps mentioned in Section 5.1 are marked with arrows.

are located in Cloud 1 and Cloud 4, i.e., 141 and 123 sources, respectively. The number of extracted clumps is similar in Cloud 2 and Cloud 5, with 33 and 36, respectively. The remaining 18 clumps are distributed in Cloud 3. The identified clumps include all 37 ATLASGAL clumps identified by Urquhart et al. (2014a) using the same SExtractor algorithm. From the present analysis, we infer that both high sensitivity and high angular resolution of the ALOHA data set allow us to detect hundreds of additional clumps located in extended diffuse background. Furthermore, the measured fluxes of the ATLASGAL clumps from previous 870 μm and our 850 μm observations are comparable within quoted uncertainties (see Appendix A.4 and Figure A6).

4.4. Physical Properties of Filaments and Clumps.

4.4.1. Width and Flux of Filaments

Although the FILFINDER algorithm gives the positions and lengths of filament skeletons, the other resulting parameters (e.g., filament width) may be biased. This is because the averaged radial intensity profiles across the filamentary skeletons are not always characterized by a Gaussian/Plummer-like function, which is usually applied to derive the filament width. This situation becomes severe for the hub-composing filaments in HFSs. For the individual filaments, we can derive the averaged radial intensity profile of each skeleton using FilFINDER, and an example of the Gaussian profile is shown in Figure 5. However, in HFSs, some hub-composing filaments display significantly different irregular profiles. In some cases, limitations in the number of sample points (i.e., short filaments or those between multiple connections such as in HFSs) may also prevent us from obtaining accurate profiles, leading to a poor determination of the filament width. To account for the above-

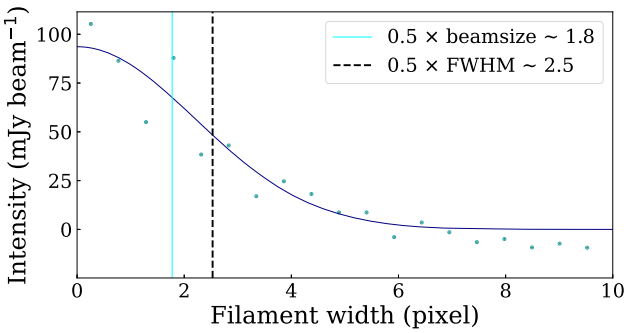

Figure 5. An example of the averaged radial profile from the FILFINDER. The solid dark blue line shows the profile fitted with a Gaussian curve. Both 0.5 × beam size and 0.5 × FWHM are presented in the plot.

mentioned inaccuracies, we adopt a common filament average width for all hub-composing filaments in HFSs.

For the total flux at 850 μm within each filament, we integrate all 850 μm intensity within a curved rectangle defined by the filament width and its length, which was assumed to represent a 2D projection of each filament. During the measurement of total flux, we did not perform large-scale background subtraction. This is because such subtraction has been carried out during our data-processing stage (as detailed in Section 3.1). To address flux uncertainties arising from a fixed filament width, we measured the total flux by varying each filament's width by $\pm1/2$ times, which will be discussed in Section 4.4.2. Note that we did not partition the hub flux into specific filaments within the HFSs. Instead, we incorporated the hub flux into the overall flux measurement for each filament composing the hub. The total integrated flux at 850 μm for each filament is listed in Column (5) of Table B1.

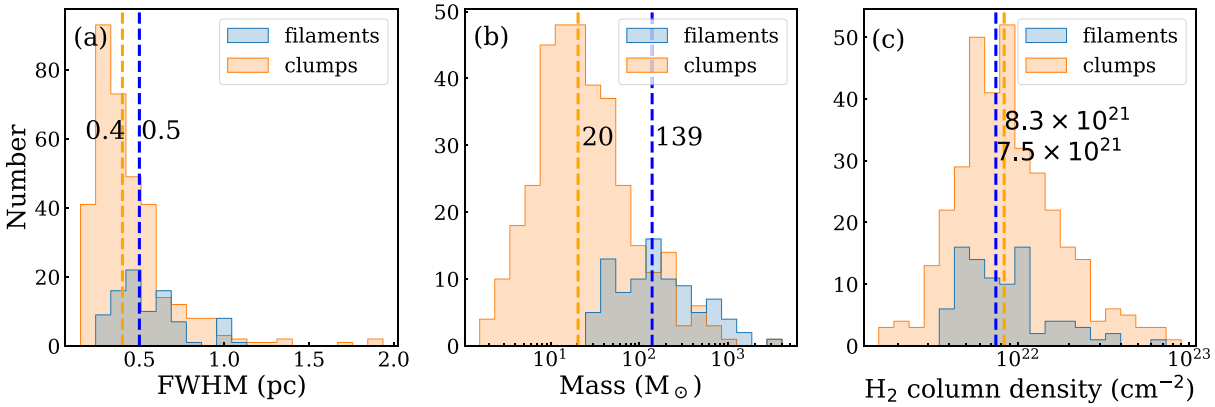

Figure 6. Distribution of parameters (i.e., FWHM, mass, column density) of filaments (blue) and clumps (orange). The corresponding median value is indicated with a vertical dashed line.

4.4.2. Dust Temperature, Mass, and Related Properties of Both Filaments and Clumps

The mass of clumps and filaments was calculated following the graybody radiation model (e.g., Hildebrand 1983; Liu et al. 2021):

$$M = \frac{D^2 S_\nu R_{\rm gd}}{B_\nu(T_{\rm dust})\kappa_\nu}, \quad (1)$$

where D is the source distance, S_ν is the integrated flux of 850 μm emission, $R_{\rm gd}$ is the gas-to-dust mass ratio taken as $R = 100$, B_ν is the Planck function for a dust temperature $T_{\rm dust}$, and κ_ν is the dust absorption coefficient taken as $\kappa_{850\,\mu{\rm m}} = 1.85$ cm^2 g^{-1}. This value was derived from the interpolation of the values listed in Column (5) of Table 1 in Ossenkopf & Henning (1994), called the OH5 model (Shirley et al. 2011). Here, $T_{\rm dust}$ was estimated from the 18″ resolution temperature map (see Figure A4 in Appendix A), which presents a range of 14 K–48 K with a median value of 18 K. It was created using the 160 μm and 250 μm images from the Hi-GAL survey, where the ratio of the two images serves as a temperature probe (see details in Peretto et al. 2016; Pan et al. 2023).

We estimated the average H_2 column density ($N_{\rm H_2}$) as follows:

$$N_{\rm H_2} = \frac{M}{A\mu_g m_{\rm H}}, \quad (2)$$

where A is the measured area of density structures (clumps or filaments), μ_g is the molecular weight per hydrogen molecule taken as 2.8 (Kauffmann et al. 2008), and $m_{\rm H}$ is the mass of a hydrogen atom.

For clumps only, their mass surface densities ($\Sigma_{\rm clump}$) were computed using the following equation:

$$\Sigma_{\rm clump} = \frac{M_{\rm clump}}{\pi R_{\rm clump}^2}, \quad (3)$$

where $M_{\rm clump}$ and $R_{\rm clump}$ represent the mass and radius of a clump, respectively. The derived parameters for the filaments and clumps are tabulated in Tables B1 and B2, respectively.

The uncertainties of these properties come from various aspects. We first consider a kinematic distance uncertainty of 10%, which is directly linked to the uncertainties of length and width of the filaments or the radius of clumps. The dust opacity (κ_ν) at the same frequency can exhibit variations across different clouds, ranging from diffuse to dense environments. This variability is observed in studies such as those by Martin et al. (2012), Roy et al. (2013), and Webb et al. (2017). Similarly, the gas-to-dust ratio ($R_{\rm gd}$) is also seen to vary. According to Sanhueza et al. (2017) and Xu et al. (2024), κ_ν may vary by approximately 28%, conservatively estimated from the OH5 model. Additionally, $R_{\rm gd}$ can deviate by 23% relative to a reference value of $R_{\rm gd} = 100$. To account for uncertainties stemming from these sources, we assumed a uniform distribution between extreme values. Employing the Monte Carlo technique with 10,000 random samples, we calculated the standard deviation as the final uncertainty in related parameter calculations.

For clumps, mass uncertainties range from 43% to 47%, with a mean value of approximately 44%. The column/surface density uncertainties span 38%–42%, with a mean value around 39%. In the case of filaments, the related uncertainties remain the same as for clumps. However, when accounting for potential variations in filament width (up to 1/2 times, see Section 4.4.1), total flux uncertainties for each filament range from 38% to 77%, resulting in higher mass uncertainties of 58%–91% with a mean value of approximately 78%.

4.4.3. Statistical Results of Physical Properties

Figure 6 shows the summary statistics of the physical properties of filaments and clumps. Figure 6(a) shows that widths of filaments have a median value of ∼0.51 pc. The width of a filament, considered as one of its fundamental properties, is subject to debate (see reviews by André et al. 2014; Hacar et al. 2023; Pineda et al. 2023). In contrast, the size distribution of clumps is wider, ranging from ∼0.25 to 2 pc, with a median value of 0.37 pc, slightly smaller than the filament width.

Figure 6(b) shows an evident difference between the distributions of the mass for filaments and clumps, with the peaks of the two types of samples clearly offset from each other. The filaments have masses of 26–2962 $M_\odot$ with a median value of 139 $M_\odot$, while the clump masses range from 2 to 4023 $M_\odot$ with a median value of 20 $M_\odot$.

Figure 6(c) displays the distributions of the averaged column density for filaments and clumps. The two distributions have a similar dynamical range, with a similar median value of $\sim 8 \times 10^{21}$ cm^{-2}.

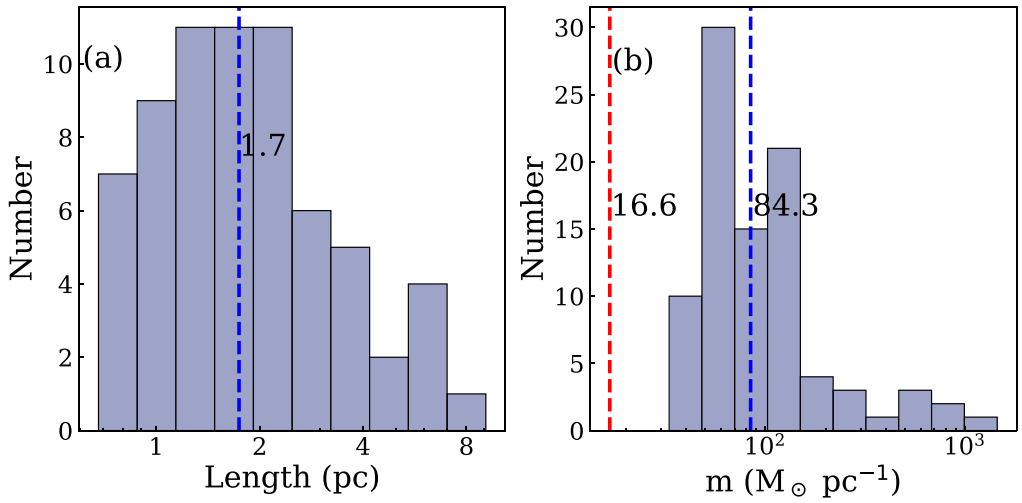

Figure 7. Length and line mass distributions of filaments. The vertical blue line in both panels represents the median value, while the red line in panel (b) gives a critical line mass of 16.6 $M_\odot$ pc^{-1}.

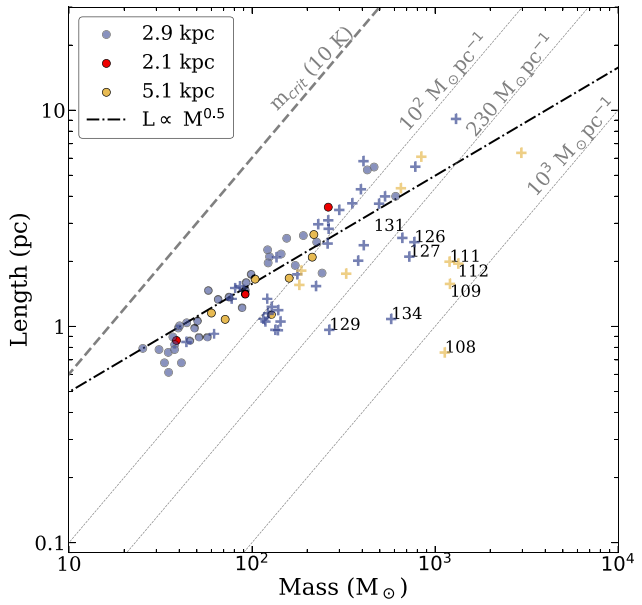

Figure 8. Mass–length diagram of individual filaments and hub-composing filaments within HFSs. The solid circles denote the individual filaments located at different distances, while the plus symbols mark the hub-composing filaments within HFSs. Numbers indicate hub-composing filaments characterized by notable deviations from the global trend (see text). The bold dashed–dotted line presents the relation $L \propto M^{0.5}$ described by the simple model of Hacar et al. (2023). The thick dashed line at the top of the diagram represents a typical critical line mass of 16.6 $M_\odot$ pc^{-1}, while the bold dashed–dotted line represents the global trend between mass and length. The light dashed lines represent different reference line masses.

Figure 7 provides the distributions of the length and line mass m of filaments. The filament length ranges from 0.7 to 9.1 pc, with a median value of 1.7 pc. The line mass m is defined as the ratio of the mass to the length of a filament in units of $M_\odot$ pc^{-1}. Overall, the observed line masses fall within the range of the statistical results reported in previous Galactic surveys, as summarized in Table 2 of Hacar et al. (2023) and references therein.

The observed line mass, in conjunction with the critical one $m_{\rm crit}$, is a standard criterion for assessing the stability of the filament. $m_{\rm crit}$ is 16.6 $M_\odot$ pc^{-1} for an ideal isothermal cylindrical model (Ostriker 1964) at a kinematic temperature of 10 K. As a result, the observed line masses are greater than the theoretical value, indicating a dynamical state of being gravitationally bound. Furthermore, we investigated the turbulent contributions for the dense filaments using the NH_3(1–1) data with a beam size of ∼32″ from the RAMPS survey (Hogge et al. 2018, and see Appendix A.5). Due to the low detection rates of the RAMPS survey across the entire G35 complex (see Figure A7), we only report the typical values in the following. We find that IR-bright Cloud 4 exhibits larger line widths (∼0.87 km s^{-1}) than the remaining relatively quiescent clouds (∼0.49 km s^{-1} for Clouds 1, 2, 3, and 5). The critical line mass $m_{\rm vir,crit}$ including the contributions of the nonthermal motions (Fiege & Pudritz 2000), also called the virial line mass, was calculated as follows:

$$m_{\rm vir,crit} = \frac{2\sigma_v^2}{G} \quad (4)$$

where σ_v is the total velocity dispersion of the gas and G is the gravitational constant. Using the two typical line widths estimated above in Equation (4), we derived two critical line masses of 352 $M_\odot$ pc^{-1} for the IR-bright cloud and 112 $M_\odot$ pc^{-1} for its IR-quiet counterparts. The latter is comparable to the observed median line mass in Figure 7, implying a considerable turbulent contribution to the dynamical stability in the early stages of filament evolution. However, in more evolved IR-bright environments, the turbulent contribution is observed to be higher by a factor of three, implying the potential role of external pressures in maintaining the dynamical stability of filaments.

4.4.4. Mass–Length Diagram

Figure 8 shows the mass–length diagram of filaments, both individual filaments (i.e., small solid circles) and hub-composing ones (i.e., plus symbols) within HFSs. We find the two populations of filaments to be differently distributed, with the hub-composing ones exhibiting a wider spread in length and mass.

In the above analysis, both parameters depend on distance. To remove the mutual dependence of mass and length on the

Table 1
Summary of Correlation Coefficients

	Entire Samples	Hub-composing Filaments
ρ_{12}	0.837	0.637
ρ_{13}	0.303	0.468
ρ_{23}	0.135	0.115
$\rho_{12,3}$	**0.844**	**0.664**

Note. "1," "2," and "3" correspond to mass, length and distance, respectively. The notation ρ_{xy} indicates the Spearman's rank correlation coefficient of each pair, while $\rho_{12,3}$ indicates the partial correlation coefficient (highlighted in bold).

distance, the first-order partial correlation test (e.g., Urquhart et al. 2018; Yang et al. 2018; Taniguchi et al. 2023) was adopted. The partial correlation coefficient, $\rho_{12,3}$, is as follows:

$$\rho_{12,3} = \frac{\rho_{12} - \rho_{13}\rho_{23}}{\sqrt{(1-\rho_{13}^2)(1-\rho_{23}^2)}}. \quad (5)$$

Here, "1" and "2" denote the two dependent parameters (mass and length, respectively) that we prioritize, while "3" signifies the independent distance that may influence them. ρ_{xy} (i.e., ρ_{12}, ρ_{13}, ρ_{23}) represents the Spearman's rank correlation coefficient between pairs. Table 1 summarizes all of the correlation coefficients for the entire samples and hub-composing filaments alone. As shown in Table 1, the correlation between mass and length is already strong in the entire sample ($\rho_{12,3} > 0.84$ with p-value $\ll 0.001$), while the hub-composing ones show relatively weaker correlations ($\rho_{12,3} \sim 0.66$ with p-value $\ll 0.001$). These results suggest that the dispersion of the mass–length distribution can mostly be attributed to the presence of hub-composing filaments. Meanwhile, the consistency between the Spearman coefficient and the partial correlation coefficient suggests that the effect of distance on the distribution of mass and length is negligible.

5. Discussion

5.1. Implication of Mass–Length Scaling of Filaments

The mass–length (M-L) diagram presented in Figure 8 shows interesting trends. All the individual filaments (small solid circles) and most of the hub-composing filaments (plus symbols not numbered) are seen to approach a global trend (but with a somewhat steeper slope), proposed by Hacar et al. (2023) as a power-law scaling relation of $L \propto M^{\alpha}$ ($\alpha = 0.5$). This scaling relation is similar to Larson's $M \propto R^2$ (Larson 1981; Solomon et al. 1987; Heyer et al. 2009) and could be attributed to turbulent fragmentation from clouds to filaments (Tafalla & Hacar 2015; Smith et al. 2016; Hacar et al. 2023). In such a turbulent fragmentation scenario, filaments increase in mass and length as they undergo turbulence-dominated either longitudinal or radial accretion from their natal clouds. As the radial accretion progresses, the length could remain nearly steady, while the mass continues to increase, likely causing a slight deviation from the global scaling relation (e.g., Feng et al. 2024). This could account for the somewhat steeper trend observed in the global distribution of most filaments, compared to the proposed relation $L \propto M^{0.5}$.

Moreover, a number of the hub-composing filaments (numbered plus symbols) are seen to significantly deviate from the aforementioned power-law scaling. This deviation is reliable since even when considering the uncertainty in the mass of the filament, which could be up to ∼80% (see Section 4.4.2), we do not anticipate a significant deviation in mass, such as an order of magnitude, when the length of the filaments is held constant. In addition, a similar deviation has been reported in the hub-composing filaments of nearby molecular clouds, such as Musca, L1495-B213 (Taurus), and Orion A (see Hacar et al. 2023). It is worth noting that these hub-composing filaments investigated here have high line masses that are greater than a threshold line mass of $230\,M_{\odot}\,\mathrm{pc}^{-1}$. This threshold indicates high-mass star formation (HMSF) as inferred by Li et al. (2016), following Equation (12) of Fiege & Pudritz (2000), using a lower limit ($0.7\,\mathrm{km\,s}^{-1}$) of line widths obtained from ammonia observations of massive star-forming clumps (Dunham et al. 2011; Urquhart et al. 2011; Wienen et al. 2012).

Furthermore, these numbered hub-composing filaments (see Figure 8) are found to be associated with H II regions (see Column (12) of Table B2). The dust temperatures of these filaments could be higher than those reported in Table B1. If the temperature were higher by a factor of two, the mass of the filament would be underestimated by the same factor. However, this would not significantly impact the evident deviation of these HFS filaments from the global trend observed in the mass–length distribution of most filaments. In light of this, these hub-composing filaments could therefore be influenced by feedback from massive star formation, such as the expansion of H II regions and bubbles. This feedback, in conjunction with ambient turbulence, acts as an external force that can condense and break up the gas. Generally, this leads to formation of more thermally supercritical filaments that compose the hub, as discussed by Shimajiri et al. (2019). Consequently, this causes the filaments to make a nearly vertical downward shift in the M-L plot.

It is important to note that the discussions above on the M-L plot may be affected by observational biases. Schisano et al. (2020) found that the filament length measured from ground-based observations is generally 2–4 times shorter than that from space-based observations given a comparable filament mass. This difference, resulting from observational biases, could potentially explain why the HFS sample provided by space-based observations does not deviate significantly from non-hub filaments in the M-L plot in Kumar et al. (2020), as opposed to the result shown here in Figure 8.

Additionally, we do not find a scaling relation (and hence not shown here) between filament density ($\langle n \rangle$) and L, similar to Larson's third relation. Hacar et al. (2023) suggested that such a relation is equivalent to the assumption of constant column density for filaments, which does not hold for our samples. This result could be due to the fact that filament densities depend on the asymmetric structure of the cylinders, and thus the density estimate under the assumption of a spherical morphology could affect the resulting $\langle n \rangle$–L relation.

5.2. HFS Clouds as a Preferential Site of HMSF

Figure 4 shows the spatial distribution of clumps along with their masses, and mass surface densities. In Figure 4(a), 75% of massive clumps ($M \geqslant 20\,M_{\odot}$) are located in the filaments, whereas low-mass clumps are distributed more widely. The HFSs have many massive clumps at the hubs. For example, the longest one (i.e., HFS8 in Figure A5) contains massive clumps

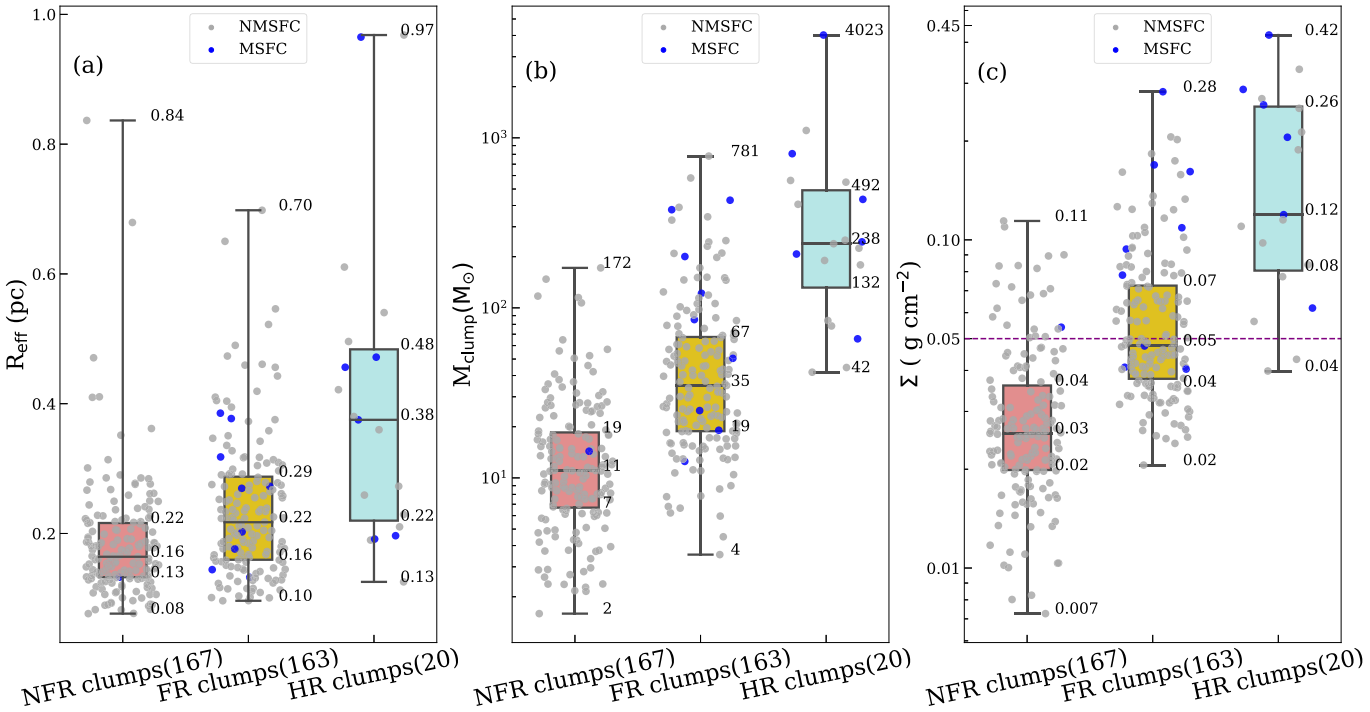

Figure 9. Box plots of the physical properties: effective radius (a), mass (b), and mass surface density (c) for three classes of clumps (i.e., NFR, FR, and HR, see the text). The numbers within the parentheses in each classification indicate the number of clumps belonging to each class. The boxes represent the quartile range of the data, from the bottom to the top of each box, including the lower quartile (i.e., the 25th percentile), the median inside the box, and the upper quartile (i.e., the 75th percentile). The "whiskers" present the full extent of the data (i.e., minimum value and maximum value). The purple dashed line in panel (c) represents a mass surface density of 0.05 g cm^{-2}. Scatter plots show the concentration of data, while whiskers represent the extent of data distribution. Different colored scatters mark the MSF clumps (MSFC) and non-MSF clumps (NMSFC).

associated with MYSOs typical of high-mass protostars, as reported by the rms survey (Urquhart et al. 2008), and includes a nascent stellar cluster G35.60-0.00 (Kuhn et al. 2021).

The mass surface density is another key parameter in star formation, especially HMSF. Thresholds for massive star formation, advocated by several authors (e.g., Krumholz & McKee 2008; Urquhart et al. 2014b), lie in the range from 0.05 g cm^{-2} to 1.0 g cm^{-2}. As shown in Figure 4(b), the mass surface densities of clumps in hubs or ridges (i.e., IRDC G35.39 and the 8 μm-bright ridge G35.6-0.0) are higher than the ATLASGAL clumps' lower limit of 0.05 g cm^{-2} (Urquhart et al. 2014b). These observed trends are in good agreement with the previous observations, which have characterized the essential roles of HFSs in massive star formation (e.g., Schneider et al. 2012; Peretto et al. 2013; Kumar et al. 2020, 2022; Arzoumanian et al. 2023).

Our observations of massive and dense clumps lying in filamentary structures or located at their junctions are qualitatively very similar to the previous results of MHD simulations (e.g., Inoue & Fukui 2013; Gómez & Vázquez-Semadeni 2014; Chen & Ostriker 2015; Gong & Ostriker 2015; Inoue et al. 2018). In these simulations, converging turbulent flows, colliding flows or cloud–cloud collisions are considered as the vital factors to produce the dense filaments and HFSs naturally. Meanwhile, the growth pattern of central clumps follows the "clump-fed" model (Smith et al. 2009) in which central massive clumps act as reservoirs of HMSF in the HFSs, gaining mass through gas accretion from their large-scale environments such as filaments. Theoretically, the GHC scenario (Vázquez-Semadeni et al. 2019) further emphasizes the pivotal role of filaments in molecular cloud evolution, where they accumulate material through radial accretion from ambient gas and feed dense clumps through longitudinal contraction.

For further analysis, we divide 350 clumps into three groups based on their location in filaments, in hubs, or in neither (see Figure 3 for example): 167 non-filament-rooted (NFR), 163 filament-rooted (FR), and 20 hub-rooted (HR) clumps. The numbers in each category could be influenced by the level of background subtraction achieved. However, this effect will not be further examined as such background subtraction was not specifically performed, except for the one incorporated during the data-processing stage (see Section 3.1). Figure 9 reveals an increasing trend of the median value for all three physical parameters (i.e., clump radius, mass, and mass surface density) from NFR to FR to HR clumps. In particular, the median value of mass surface density increases by a factor of 4 from NFR to FR to HR clumps, while that for mass increases by a factor of 17. The observed trends persist even if we account for the uncertainty of around 10% for the radius of clumps, around 44% for the mass, and around 39% for the mass surface density (see Section 4.4.2). In addition, similar increasing trends of clump radius/mass from the NFR clumps and FR clumps were also found in the study of cores in Orion (Polychroni et al. 2013). To evaluate such increasing trends further, we applied the Kruskal–Wallis H test, which can infer the difference among the distributions of multiple independent samples from different populations. The null hypothesis usually assumes that the samples come from the same parent population. Table 2 shows the p-values and χ^2 of the Kruskal–Wallis H test for physical parameters of one group against others. Since the p-values of all cases are much lower than 0.05, we reject the null

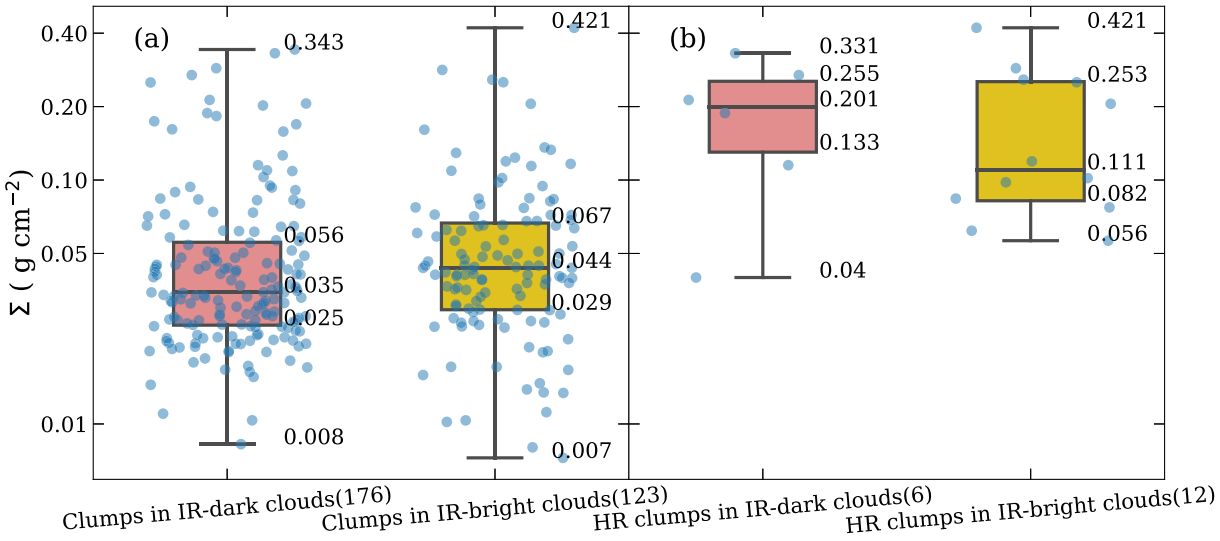

Figure 10. Box plots for comparison of mass surface density between clumps in an IR-dark environment (i.e., in Cloud 1 and/or Cloud 2) and those in an IR-bright environment (i.e., in Cloud 4). (a) Comparison between clumps in IR-dark Clouds 1 and 2 and those in IR-bright Cloud 4. (b) Distribution of mass surface density of HR clumps (i.e., those located at hubs) in both IR-dark (i.e., in Clouds 1 and 2) and IR-bright (i.e., in Cloud 4) environments. The numbers in parentheses of the horizontal axis labels represent the sample counts in each group.

Table 2
Kruskal–Wallis H Test Results of Clump Properties for Three Groups: NFR, FR, and HR Clumps

Property group	R (pc)	M ($M_\odot$)	Σ (g cm $^{-2}$)
p-value	1.8×10^{-11}	2.6×10^{-30}	2.3×10^{-31}
χ^2	49.5	136.3	141.1

Note. If p-value is smaller than the significance level, the null hypothesis will be rejected. A larger χ^2 indicates a more significant difference between different groups.

hypothesis, and conclude that all three classification groups of clumps have different distributions, in terms of the radius, mass, and mass surface density parameters. Therefore, the observed increasing trends of these three parameters from NFR to FR to HR clumps could be significant. Accordingly, these trends underscore the tendency for massive dense clumps to associate with filaments and HFSs. In particular, the densest HR clumps offer conducive conditions for HMSF, indicating HFSs as preferential sites for such star formation.

We also used different tracers from previous catalogs, such as class II methanol masers, MYSOs, and ultracompact H II regions, to match our clumps with signposts of massive star formation. As a result, we identified 16 such massive star-forming (MSF) clumps. Among them, 15 preferentially reside in filaments or in the hubs within HFSs (see Figure 9). Although the counts of high-mass star-forming clumps are similar between the HFS's hubs and the isolated filaments, the former has a much higher fraction of the observed population than the latter does. This quantitative analysis favors the importance of filaments in HMSF, and even the HFS clouds as a preferential site of HMSF.

5.3. Evolution of Clump Density

We select the distance-independent parameter of clump mass surface density to examine how critical parameters of HMSF evolve in different star-forming environments. For this analysis, we focus on clouds with evident IR-dark and IR-bright signatures. The presence of IRDCs (i.e., G35.39 and G35.41) suggests quiescent star formation in Clouds 1 and 2. In comparison, the detection of several H II regions (Anderson et al. 2014) in Cloud 4, which are seen as IR-bright signatures, indicates current star formation activity, and a relatively later evolutionary phase (see Section 2). Given the weak 850 μm emission in Cloud 3 and Cloud 5 relative to other clouds, these have been excluded from the discussion here.

Figure 10(a) shows a comparison of the densities of the clumps located at two different evolutionary stages of clouds at different distances (IR-dark Clouds 1 and 4 versus IR-bright Cloud 4). As seen in Figure 10(a), the mass surface densities of clumps are slightly higher in the IR-bright clouds than in their IR-dark counterparts with a median ratio of 1.3. We conduct a two-sample Kolmogorov–Smirnov (K-S) test to investigate whether they are statistically identical. The statistical results, yielding a p-value of less than $\sim$0.005, suggest that the samples are unlikely to be drawn from the same parent population. The weak trend implies a possible increasing trend for the mass surface density of clumps from the IR-dark to IR-bright stage. In their statistical study of a sample of 17 HFS clouds using data from the Atacama Large Millimeter/submillimeter Array, Liu et al. (2023) have observed a similar increasing trend (by a factor of around 3) in the central massive clumps from IR-dark to IR-bright HFSs. Several other systematic studies (e.g., Giannetti et al. 2013; Urquhart et al. 2014b; Rigby et al. 2021; Xu et al. 2024) also conjecture a similar positive correlation of density as a function of evolutionary sequence. It is also worth noting that there are other studies (e.g., López-Sepulcre et al. 2010; Rathborne et al. 2010; Sánchez-Monge et al. 2013), where no significant differences in column densities (equivalent to surface densities) were observed for clumps. Furthermore, clumps in the H II region phase show an even greater difference in surface densities than the other stages (e.g., Urquhart et al. 2014b; He et al. 2015). In contrast, Guzmán et al. (2015) presented results of 3000 massive MALT90 clumps in disagreement with the

previous enhanced densities in the group of H II regions. Their study shows that the surface density of clumps tends to decrease during the development of H II regions. Note that the observed trend should be treated with caution, given the estimated uncertainties (see Sections 4.4.2 and 5.2).

If we consider the HR clumps depicted in Figure 10(b), these massive structures, rooted in the central hub of HFS clouds, exhibit a decreasing surface density trend from an IR-dark to an IR-bright stage, contrasting with the previously mentioned weak increasing trend. A two-sample K-S test also conducted on the two groups yielded a p-value of 0.76, suggesting a common origin. Consequently, the observed decreasing trend should be interpreted with caution. Under the framework of the latest theoretical models like GHC and I2, HMSF in HFSs involves a multiscale mass accretion/transfer process from the cloud to filaments and then onto the central hub and finally to the star-forming cores. Thus, clumps located in the central hubs would be in a state of active accretion, increasing in mass and mass surface density. However, for HR clumps in IR-bright clouds, 11 out of the 12 clumps are associated with H II regions. In this phase, ionizing feedback and radiation pressure from MYSOs would play an important role in influencing the temporal trend of mass surface density in these clumps. Given the critical role of this trend in understanding mass accretion and HMSF, further dedicated observational studies are warranted.

6. Conclusions

In this paper, we have carried out a systematic analysis on the filaments and their hierarchically fragmented clumps in the G35 molecular complex, centered at $\alpha_{2000} = 18^{h}56^{m}28^{s}.16$, $\delta_{2000} = 2°14'25.''71$, with an approximate radius of $0.^{\circ}41$ from SCUBA-2 850 μm continuum observations. We focus on the basic physical properties of the filaments and clumps, including their mass, density, and size. The major results are as follows.

(1) Five clouds, namely Clouds 1–5, were identified. Their respective kinematic distances, estimated from the ^{13}CO(1–0) line data, are 2.9 kpc, 5.1 kpc, 2.9 kpc, 2.9 kpc, and 2.1 kpc.
(2) We extracted a sample of 91 filaments, some of which can be divided into 10 HFSs, each composed of at least three hub-composing filaments. A catalog of 350 dense clumps was compiled, 183 of which are associated with the filaments.
(3) The identified filaments have a median width of 0.51 pc, lengths ranging from 0.7 pc to 9.1 pc, and masses between ∼26 and 2962 $M_{\odot}$. All exceed the thermally critical line mass of 16.6 $M_{\odot}$ pc^{-1}, with a median value of 84 $M_{\odot}$ pc^{-1}. The clumps, with a median size of ∼0.4 pc and mass of ∼20 $M_{\odot}$, have a similar average column density to the filaments, suggesting a density inheritance from larger-scale filaments.
(4) The global mass–length trend of filaments, close to $L \propto M^{0.5}$, suggests that their physical origin is linked to turbulence. The hub-composing filaments within HFSs deviate from the global mass–length trend, which could be due to feedback from massive star formation therein, particularly H II regions.
(5) Massive clumps, which most likely form high-mass stars, are the densest in filaments and in the hubs of HFSs, with the latter bearing a higher probability of occurrence of high-mass star-forming signatures, favoring the HFSs as a preferential site of HMSF.
(6) We examined the variation in clumps' mass surface density relative to their host cloud environment, from the IR-dark to IR-bright stage. No significant variation was observed. This could be attributed to the regulation of clump properties, such as mass surface density, by the interplay between mass accretion and feedback from H II regions.

Overall, we have provided filament and dense clump samples in the G35 molecular complex to explore their connection with star formation. The significance of filaments, especially hub-composing filaments in HFSs, for HMSF is highlighted. Further observational studies particularly on kinematics and dynamics are needed to understand the mass accretion process in HMSF through these density structures.

Acknowledgments

This work has been supported by the National Key R&D Program of China (No. 2022YFA1603101). X.-J. Shen is supported by the 15th Graduate Student Research and Innovation Project of Yunnan University (Project ID:KC-23233964). H.-L. Liu is supported by National Natural Science Foundation of China (NSFC) through the grant No. 12103045, by Yunnan Fundamental Research Project (grant No. 202301AT070118, 202401AS070121), and by Xingdian Talent Support Plan–Youth Project. H.B.L. is supported by the National Science and Technology Council (NSTC) of Taiwan (grant Nos. 111-2112-M-110-022-MY3). P.S. was partially supported by a Grant-in-Aid for Scientific Research (KAKENHI Number JP22H01271 and JP23H01221) of JSPS. The work of M.G.R. is supported by NOIRLab, which is managed by the Association of Universities for Research in Astronomy (AURA) under a cooperative agreement with the National Science Foundation. K.T. was supported by JSPS KAKENHI (grant No. JP20H05645).

Software: Starlink (Currie et al. 2014), Astropy (Astropy Collaboration et al. 2013), FILFINDER (Koch & Rosolowsky 2015), Aplpy (Lisa & Bot 2017), Source Extractor (Bertin & Arnouts 1996; Barbary 2016)

Appendix A
Complementary Figures

A.1. Noise Map Analysis of 850 μm Dust Observations

Figure A1 displays the spatial distribution of the noise map (left panel) and the associated statistics (right panel).

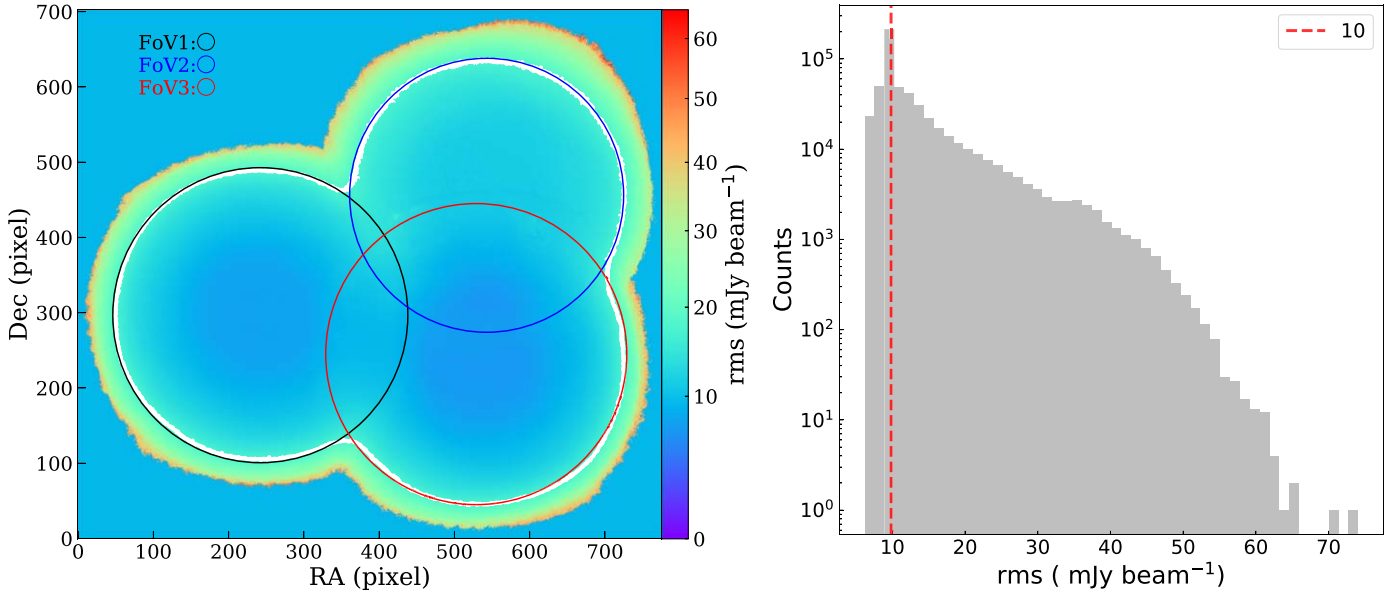

Figure A1. Noise map and statistical histogram of the rms. Left: the color map presents the rms varying from 5 to 75 mJy beam^{-1} and the white contour indicates rms value of 20 mJy beam^{-1}. The colored circles pinpoint three FOVs considered for analysis. Right: the histogram shows the distribution of the rms with a median value of 10 mJy beam^{-1} (red dashed line).

A.2. Molecular Gas Distribution in the G35 Complex

To approximately identify each cloud in the G35 molecular complex, we provide in Figure A2 the average spectrum of ^{13}CO ($J = 1$–0) over the entire complex, and in Figure A3 the JCMT 850 μm continuum image overlaid with the intensity contours of ^{13}CO for each individual cloud.

A.3. Spatial Distribution of Dust Filamentary Structures in the G35 Complex

Figure A4 shows the filamentary structures identified in Section 4.3.1 overlaid on the dust temperature map. Figure A5 presents the spatial distribution of 10 HFSs overlaid on the Spitzer 8 μm infrared image.

A.4. Flux Comparison of the Clumps Observed Both in Previous 870 μm and our 850 μm Observations

We examined the variance in peak flux density of the 37 matched clumps between the two catalogs from the ATLASGAL survey (Urquhart et al. 2018) at 870 μm and our own at 850 μm. Owing to the higher angular resolution (14″) of our observations, we recalibrated the 850 μm peak flux density to match the angular resolution (19″) at 870 μm. This recalibrated value of the 850 μm peak flux density was then utilized to predict the 870 μm peak flux density using a power-law relation ($S_\nu \propto \nu^\alpha$) and a spectral index $\alpha = -2$. Figure A6 illustrates the comparison between the 870 μm peak flux density observed from the ATLASGAL survey and the result predicted from our 850 μm observations. The peak flux densities display a strong linear correlation with a Pearson correlation coefficient of 0.99, with the predicted flux densities exceeding the observed ones by approximately 21%. This implies that the flux measurements for clump sources are consistent between the previous 870 μm and our 850 μm observations, considering the systematic flux uncertainties of about 15% in the former (e.g., Schuller et al. 2009) and about 6% in the latter (see Section 3.1).

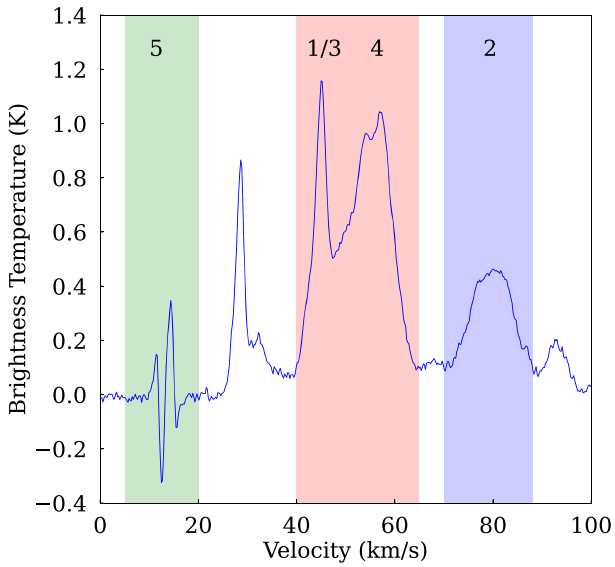

Figure A2. Average spectrum of ^{13}CO(1–0) emission over the G35 molecular complex. The colored bands highlight three major velocity components, corresponding to [5, 20], [40, 65], and [70, 85] km s^{-1} in green, red, and blue, respectively. The numbers represent the cloud IDs.

A.5. NH_3(1–1) Data Selected for Filament Kinematic Analysis

Higher-J CO line data are assumed to be superior for tracing filament kinematics than the CO $J = 1$–0 line observed for example in the FUGIN (Umemoto et al. 2017) and GRS

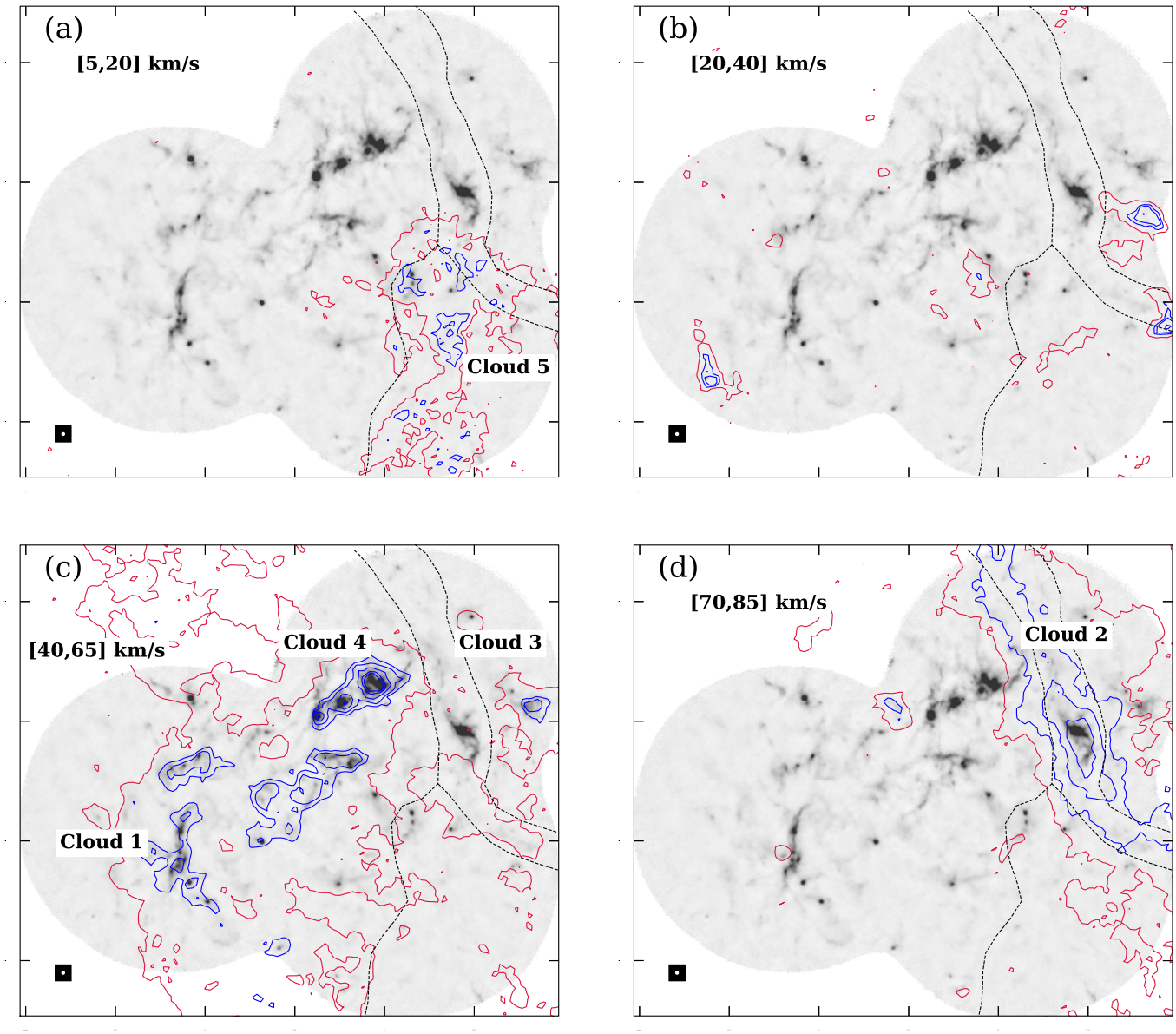

Figure A3. JCMT 850 μm continuum image overlaid with ^{13}CO integrated intensity contours of different velocity components. They correspond to [5, 20], [40, 65], and [70, 85] km s^{-1}. The rms levels (σ) of the four integrated intensities from (a) to (d) are $\sigma_1 = 0.73$ K km s^{-1}, $\sigma_2 = 0.72$ K km s^{-1}, $\sigma_3 = 2.82$ K km s^{-1}, and $\sigma_4 = 1.28$ K km s^{-1}, respectively. The red contour in each panel indicates the the 5σ level. The blue contour levels from panel (a) to (b) are [$8\sigma_1$, $10\sigma_1$] K km s^{-1}, [$8\sigma_2$, $10\sigma_2$, $15\sigma_2$] K km s^{-1}, [$10\sigma_3$, $12\sigma_3$, $15\sigma_3$, $18\sigma_3$, $20\sigma_3$] K km s^{-1}, and [$10\sigma_4$, $15\sigma_4$, $20\sigma_4$] K km s^{-1}, respectively. According to the spatial association between gas and continuum emission, boundaries of different clouds are delineated by the black dashed lines. The beam size of 850 μm observations is also displayed at the bottom left corner of each panel.

(Jackson et al. 2006) surveys. This arises from their enhanced accessibility to the dense filament's physical properties, due to their higher critical excitation density. Furthermore, for the G35 complex there are NH_3 line data from the RAMPS (Hogge et al. 2018) survey, which has an angular resolution of 32″. Despite the low detection rate of the NH_3 line data in the G35 complex, similar to higher-J CO line data, the NH_3 line is assumed to be more sensitive to the kinematics of dense gas than other lines available here. Consequently, we utilize the RAMPS NH_3 line data to approximately quantify the contribution of turbulence. Figure A7 displays the line width distribution of this species toward the G35 molecular complex.

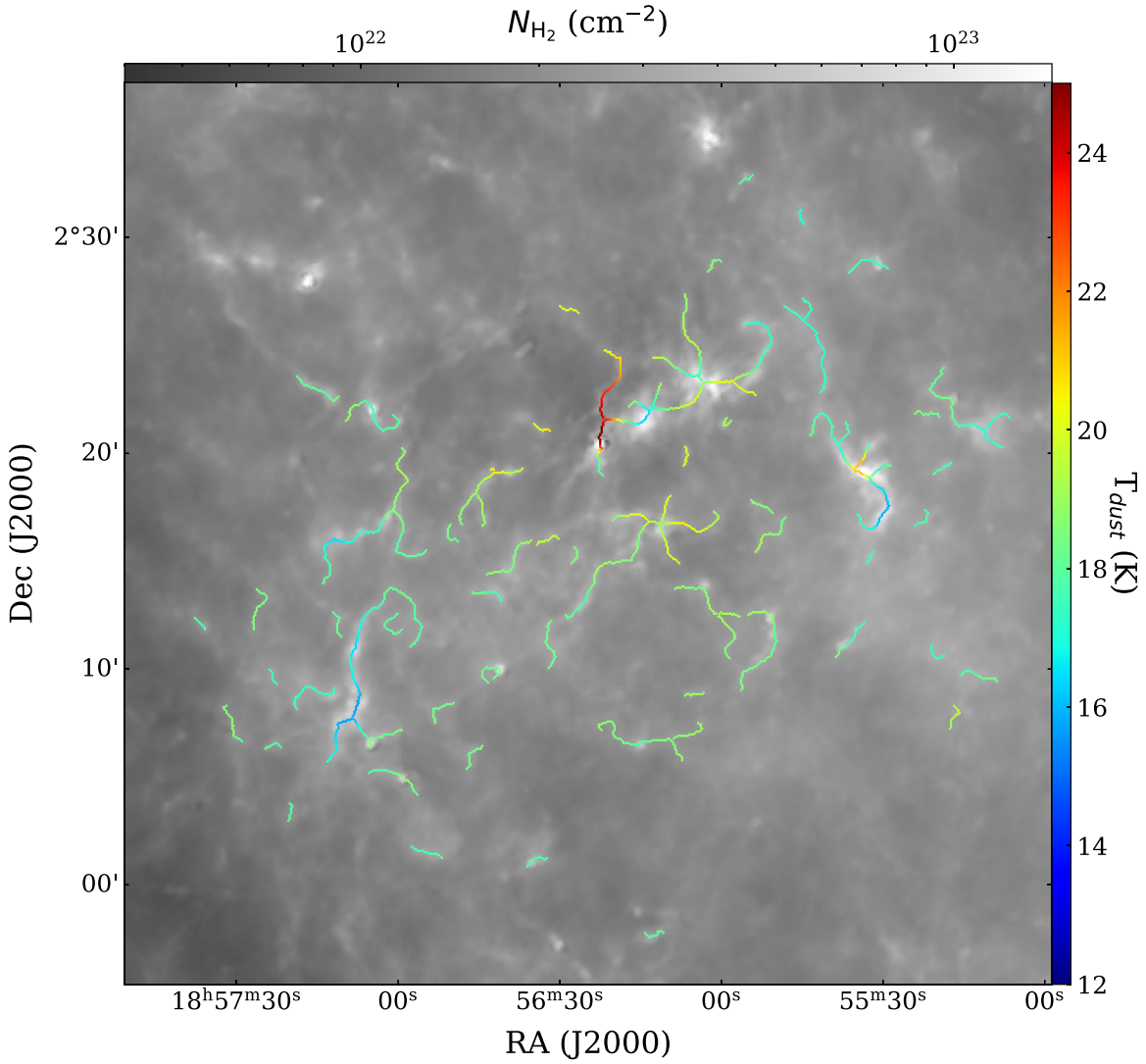

Figure A4. Filament skeletons overlaid on the column density map. The color of each structure represents its average dust temperature derived from Herschel observations.

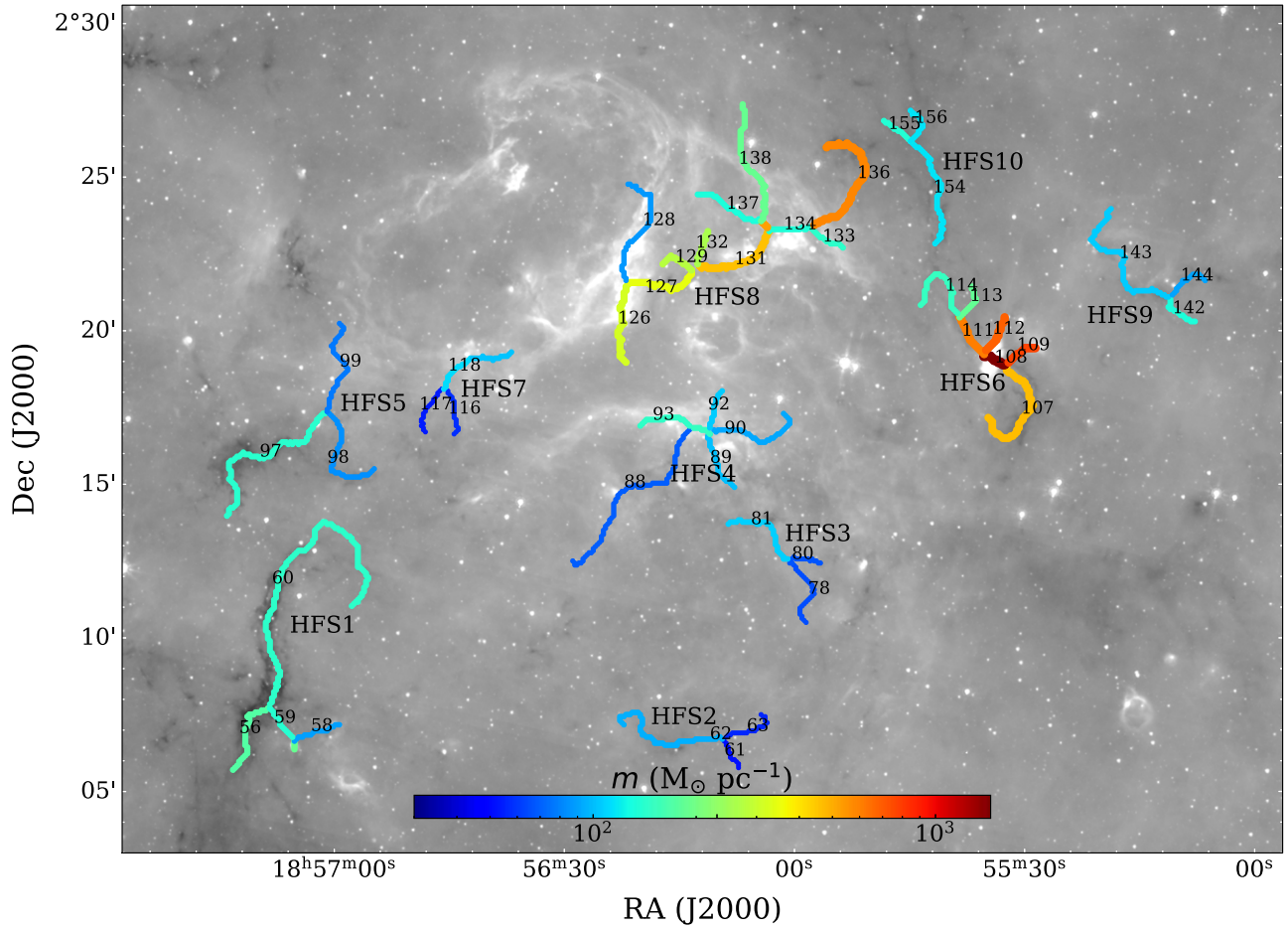

Figure A5. Spatial distribution of HFSs overlaid on the Spitzer 8 μm image. The different colored curves sketch the filaments composing HFSs, with each color indicating its respective line mass.

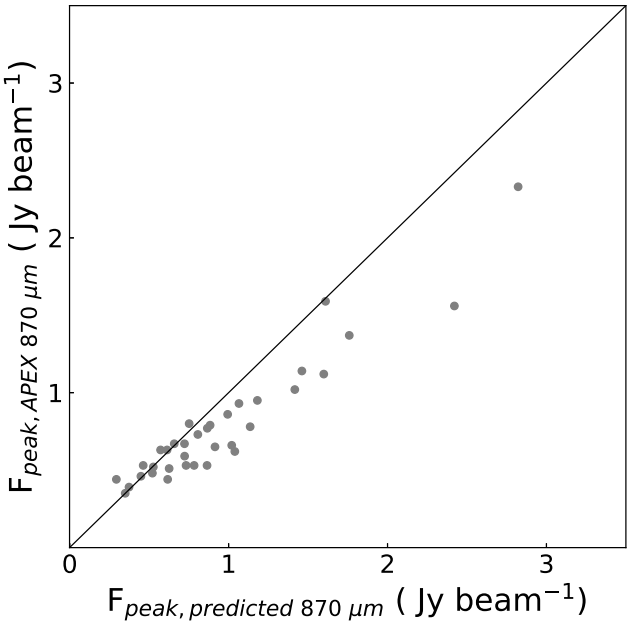

Figure A6. Comparison of peak flux density of matched ATLASGAL clumps at 870 μm and predicted results from our observed 850 μm dust emission. The black line indicates equality.

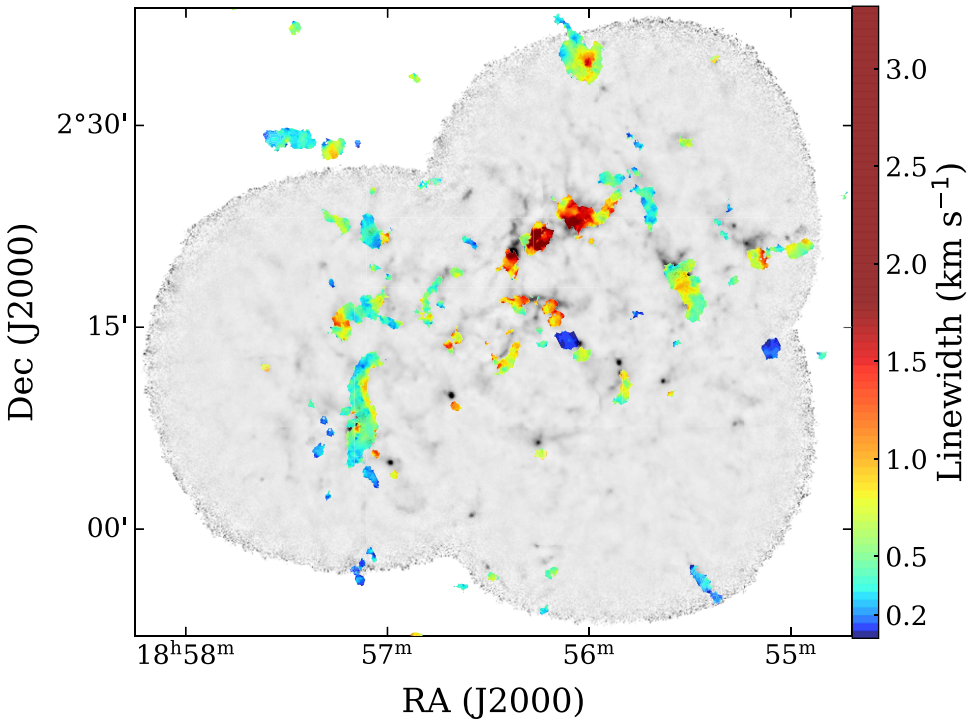

Figure A7. NH_3(1–1) line width (rainbow colors) overlaid on 850 μm continuum map (gray).

Appendix B
Complementary Tables

We list the tables of detailed parameters for the clumps and filaments. Table B1 gives basic information on each filament, the resultant physical properties for statistical analysis, and their association (Assoc.) with both HMSF and HFSs. Table B2 presents the basic parameters of 350 clumps, including their position, position angle (PA), flux, distance, as well as the derived physical parameters such as mass and surface density.

Table B1
Parameters of Filamentary Structures

ID	Name	R.A. (deg)	Decl. (deg)	Flux (mJy)	D (kpc)	Mass ($M_\odot$)	Length (pc)	Width (pc)	T_{dust} (K)	N_{H_2} (10^{21} cm^{-2})	Assoc.	Group
(1)	(2)	(3)	(4)	(5)	(6)	(7)	(8)	(9)	(10)	(11)	(12)	(13)
44	G35.220-0.164	284.049	1.962	868 ± 347	2.9	50 ± 29	1.0	0.3	17.3	8.6 ± 4.7	-	-
46	G35.312-0.216	284.137	2.020	1032 ± 671	2.9	59±46	0.9	0.3	17.4	8.7 ± 6.5	-	-
47	G35.358-0.294	284.228	2.025	1352 ± 641	2.9	77 ± 49	1.4	0.3	17.4	7.3 ± 4.4	-	-
51	G35.433-0.373	284.333	2.055	465 ± 206	2.9	26 ± 16	0.8	0.3	17.6	4.9 ± 2.8	-	-
54	G35.433-0.306	284.273	2.086	4325 ± 2393	2.9	232 ± 161	2.5	0.5	18.1	8.5 ± 5.7	-	-
55	G35.411-0.229	284.195	2.102	1269 ± 916	2.9	67 ± 56	1.3	0.4	18.2	5.3 ± 4.3	-	-
56	G35.470-0.315	284.298	2.115	6412 ± 4680	2.9	408 ± 350	2.4	0.4	15.9	19.0 ± 16.0	D	HFS1
58	G35.454-0.280	284.259	2.116	2300 ± 1679	2.9	121 ± 106	1.3	0.4	18.0	10.1 ± 8.4	Y	HFS1

Note. Column (12) shows the filaments that are linked to massive star-forming sources summarized in Figure 1. The letter "D" denotes the IRDCs, "Y" represents the MYSOs, "H" marks the H II regions, and "M" stands for class II methanol masers. "Group" indicates the structures to which the filaments belong. "-" indicates individual filaments, and the designation of the HFS to which the hub-composing filaments belong is also marked. The structure with ID 108 (belongs to HFS6) shows its width slightly greater than its length due to its location in a very bright H II region (see Figure A5). The relative uncertainty of parameters of both length and width is 10%.

Table B1 is published in its entirety in the machine-readable format. A portion is shown here for guidance regarding its form and content.

(This table is available in its entirety in machine-readable form in the online article.)

Table B2
Physical Parameters of Dense Clumps

ID	R.A.	Decl.	Size	PA	R	Flux	$F_{\rm peak}$	S/N	D	$T_{\rm dust}$	Mass	Σ	$N_{\rm H_2}$
	(deg)	(deg)	(arcsec × arcsec)	(deg)	(pc)	(mJy)	(mJy beam^{-1})		(kpc)	(K)	($M_\odot$)	(g cm^{-2})	(10^{21} cm^{-2})
(1)	(2)	(3)	(4)	(5)	(6)	(7)	(8)	(9)	(10)	(11)	(12)	(13)	(14)
1	283.869	1.951	18.4 × 14.3	−50.4	0.1	300 ± 46	163	11	2.1	17.2	9 ± 4	0.09 ± 0.036	19.0 ± 7.7
2	284.056	1.959	21.7 × 15.9	−3.8	0.1	320 ± 47	148	13	2.9	16.9	19 ± 9	0.07 ± 0.03	15.8 ± 6.3
3	284.042	1.978	27.5 × 13.7	−11.7	0.1	151 ± 26	95	11	2.9	18.2	8 ± 4	0.03 ± 0.012	6.1 ± 2.5
4	283.968	1.975	21.4 × 14.4	47.9	0.1	88 ± 16	51	8	2.1	18.6	2 ± 1	0.02 ± 0.008	4.2 ± 1.8
5	284.066	1.979	19.9 × 14.1	−44.7	0.1	328 ± 39	196	21	2.9	18.3	17 ± 8	0.08 ± 0.033	17.8 ± 7.0
6	283.931	2.002	25.2 × 14.3	−75.3	0.1	109 ± 19	48	9	2.1	18.8	3 ± 1	0.02 ± 0.009	4.4 ± 1.8
7	284.145	2.019	30.3 × 17.0	20.5	0.2	834 ± 104	367	25	2.9	17.2	48 ± 22	0.13 ± 0.05	26.9 ± 10.6
8	283.962	2.025	28.9 × 15.7	58.2	0.1	103 ± 18	45	10	2.1	19.3	3 ± 1	0.01 ± 0.006	3.1 ± 1.3

Note. The relative uncertainty of parameters of both length and width is 10%.
Table B2 is published in its entirety in the machine-readable format. A portion is shown here for guidance regarding its form and content.
(This table is available in its entirety in machine-readable form in the online article.)

ORCID iDs

Xianjin Shen https://orcid.org/0009-0004-3244-3508
Hong-Li Liu https://orcid.org/0000-0003-3343-9645
Zhiyuan Ren https://orcid.org/0000-0003-4659-1742
Anandmayee Tej https://orcid.org/0000-0001-5917-5751
Di Li https://orcid.org/0000-0003-3010-7661
Hauyu Baobab Liu https://orcid.org/0000-0003-2300-2626
Gary A. Fuller https://orcid.org/0000-0001-8509-1818
Jinjin Xie https://orcid.org/0000-0002-2738-146X
Patrick M. Koch https://orcid.org/0000-0003-2777-5861
Fengwei Xu https://orcid.org/0000-0001-5950-1932
Patricio Sanhueza https://orcid.org/0000-0002-7125-7685
R. K. Yadav https://orcid.org/0000-0002-6740-7425
Busaba H. Kramer https://orcid.org/0000-0001-8168-5141
Mark G. Rawlings https://orcid.org/0000-0002-6529-202X
Chang Won Lee https://orcid.org/0000-0002-3179-6334
Daniel Harsono https://orcid.org/0000-0001-6307-4195
David Eden https://orcid.org/0000-0002-5881-3229
Woojin Kwon https://orcid.org/0000-0003-4022-4132
Chao-Wei Tsai https://orcid.org/0000-0002-9390-9672
Glenn J. White https://orcid.org/0000-0002-7126-691X
Kee-Tae Kim https://orcid.org/0000-0003-2412-7092
Tie Liu https://orcid.org/0000-0002-5286-2564
Ke Wang https://orcid.org/0000-0002-7237-3856
Wenyu Jiao https://orcid.org/0000-0001-9822-7817
Jingwen Wu https://orcid.org/0000-0001-7808-3756

References

Anderson, L. D., Bania, T. M., Balser, D. S., et al. 2014, ApJS, 212, 1
André, P., Di Francesco, J., Ward-Thompson, D., et al. 2014, in Protostars and Planets VI, ed. H. Beuther et al. (Tucson, AZ: Univ. Arizona Press), 27
André, P., Men'shchikov, A., Bontemps, S., et al. 2010, A&A, 518, L102
Arzoumanian, D., Arakawa, S., Kobayashi, M. I. N., et al. 2023, ApJL, 947, L29
Astropy Collaboration, Robitaille, T. P., Tollerud, E. J., et al. 2013, A&A, 558, A33
Barbary, K. 2016, JOSS, 1, 58
Barnes, A. T., Henshaw, J. D., Fontani, F., et al. 2021, MNRAS, 503, 4601
Barnes, A. T., Kong, S., Tan, J. C., et al. 2016, MNRAS, 458, 1990
Benjamin, R. A., Churchwell, E., Babler, B. L., et al. 2003, PASP, 115, 953
Bertin, E., & Arnouts, S. 1996, A&AS, 117, 393
Bronfman, L., Nyman, L. A., & May, J. 1996, A&AS, 115, 81
Brunthaler, A., Menten, K. M., Dzib, S. A., et al. 2021, A&A, 651, A85
Chen, C.-Y., & Ostriker, E. C. 2015, ApJ, 810, 126
Contreras, Y., Schuller, F., Urquhart, J. S., et al. 2013, A&A, 549, A45
Currie, M. J., Berry, D. S., Jenness, T., et al. 2014, in ASP Conf. Ser. 485, Astronomical Data Analysis Software and Systems XXIII, ed. N. Manset & P. Forshay (San Francisco, CA: ASP), 391
Dunham, M. K., Robitaille, T. P., Evans, Neal, J. I., et al. 2011, ApJ, 731, 90
Dzib, S. A., Yang, A. Y., Urquhart, J. S., et al. 2023, A&A, 670, A9
Feng, J., Smith, R. J., Hacar, A., Clark, S. E., & Seifried, D. 2024, MNRAS, 528, 6370
Fiege, J. D., & Pudritz, R. E. 2000, MNRAS, 311, 85
Giannetti, A., Brand, J., Sánchez-Monge, Á., et al. 2013, A&A, 556, A16
Gómez, G. C., & Vázquez-Semadeni, E. 2014, ApJ, 791, 124
Gong, M., & Ostriker, E. C. 2015, ApJ, 806, 31
Guzmán, A. E., Sanhueza, P., Contreras, Y., et al. 2015, ApJ, 815, 130
Hacar, A., Clark, S. E., Heitsch, F., et al. 2023, in ASP Conf. Ser. 534, Protostars and Planets VII, ed. S. Inutsuka et al. (San Francisco, CA: ASP), 153
He, Y.-X., Liu, H.-L., Tang, X.-D., et al. 2023, ApJ, 957, 61
He, Y.-X., Zhou, J.-J., Esimbek, J., et al. 2015, MNRAS, 450, 1926
Heyer, M., Krawczyk, C., Duval, J., & Jackson, J. M. 2009, ApJ, 699, 1092
Hildebrand, R. H. 1983, QJRAS, 24, 267
Hogge, T., Jackson, J., Stephens, I., et al. 2018, ApJS, 237, 27
Hou, L. G., & Han, J. L. 2014, A&A, 569, A125
Hu, B., Menten, K. M., Wu, Y., et al. 2016, ApJ, 833, 18
Inoue, T., & Fukui, Y. 2013, ApJL, 774, L31
Inoue, T., Hennebelle, P., Fukui, Y., et al. 2018, PASJ, 70, S53
Jackson, J. M., Rathborne, J. M., Shah, R. Y., et al. 2006, ApJS, 163, 145
Jayasinghe, T., Dixon, D., Povich, M. S., et al. 2019, MNRAS, 488, 1141
Jiao, S., Lin, Y., Shui, X., et al. 2022, SCPMA, 65, 299511
Jiménez-Serra, I., Caselli, P., Fontani, F., et al. 2014, MNRAS, 439, 1996
Kalcheva, I. E., Hoare, M. G., Urquhart, J. S., et al. 2018, A&A, 615, A103
Kauffmann, J., Bertoldi, F., Bourke, T. L., Evans, N. J. I., & Lee, C. W. 2008, A&A, 487, 993
Koch, E. W., & Rosolowsky, E. W. 2015, MNRAS, 452, 3435
Krumholz, M. R., & McKee, C. F. 2008, Natur, 451, 1082
Kuhn, M. A., de Souza, R. S., Krone-Martins, A., et al. 2021, ApJS, 254, 33
Kumar, M. S. N., Arzoumanian, D., Men'shchikov, A., et al. 2022, A&A, 658, A114
Kumar, M. S. N., Palmeirim, P., Arzoumanian, D., & Inutsuka, S. I. 2020, A&A, 642, A87
Ladeyschikov, D. A., Bayandina, O. S., & Sobolev, A. M. 2019, AJ, 158, 233
Larson, R. B. 1981, MNRAS, 194, 809
Li, G.-X., Urquhart, J. S., Leurini, S., et al. 2016, A&A, 591, A5
Li, Q., Zhou, J., Esimbek, J., et al. 2018, ApJ, 867, 167
Lisa, M., & Bot, H. 2017, My Research Software, v2.0.4, Zenodo, doi:10.5281/zenodo.1234
Liu, H. B., Jiménez-Serra, I., Ho, P. T. P., et al. 2012a, ApJ, 756, 10
Liu, H. B., Quintana-Lacaci, G., Wang, K., et al. 2012b, ApJ, 745, 61
Liu, H.-L., Liu, T., Evans, N. J. I., et al. 2021, MNRAS, 505, 2801
Liu, H.-L., Sanhueza, P., Liu, T., et al. 2020, ApJ, 901, 31
Liu, H.-L., Stutz, A., & Yuan, J.-H. 2019, MNRAS, 487, 1259
Liu, H.-L., Tej, A., Liu, T., et al. 2022, MNRAS, 510, 5009
Liu, H.-L., Tej, A., Liu, T., et al. 2023, MNRAS, 522, 3719
Liu, T., Li, P. S., Juvela, M., et al. 2018, ApJ, 859, 151
López-Sepulcre, A., Cesaroni, R., & Walmsley, C. M. 2010, A&A, 517, A66
Lu, X., Zhang, Q., Liu, H. B., Wang, J., & Gu, Q. 2014, ApJ, 790, 84
Lu, X., Zhang, Q., Liu, H. B., et al. 2018, ApJ, 855, 9
Mairs, S., Dempsey, J. T., Bell, G. S., et al. 2021, AJ, 162, 191
Martin, P. G., Roy, A., Bontemps, S., et al. 2012, ApJ, 751, 28
Molinari, S., Swinyard, B., Bally, J., et al. 2010, PASP, 122, 314
Motte, F., Bontemps, S., & Louvet, F. 2018, ARA&A, 56, 41
Myers, P. C. 2009, ApJ, 700, 1609
Nguyen, H., Rugel, M. R., Murugeshan, C., et al. 2022, A&A, 666, A59
Nguyen Luong, Q., Motte, F., Hennemann, M., et al. 2011, A&A, 535, A76
Ossenkopf, V., & Henning, T. 1994, A&A, 291, 943
Ostriker, J. 1964, ApJ, 140, 1056
Ouyang, X.-J., Chen, X., Shen, Z.-Q., et al. 2019, ApJS, 245, 12
Padoan, P., Pan, L., Juvela, M., Haugbølle, T., & Nordlund, Å. 2020, ApJ, 900, 82
Pan, S., Liu, H.-L., & Qin, S.-L. 2023, MNRAS, 519, 3851
Pan, S., Liu, H.-L., & Qin, S.-L. 2024, ApJ, 960, 76
Peretto, N., & Fuller, G. A. 2009, A&A, 505, 405
Peretto, N., Fuller, G. A., André, P., et al. 2014, A&A, 561, A83
Peretto, N., Fuller, G. A., Duarte-Cabral, A., et al. 2013, A&A, 555, A112
Peretto, N., Lenfestey, C., Fuller, G. A., et al. 2016, A&A, 590, A72
Pineda, J. E., Arzoumanian, D., Andre, P., et al. 2023, in ASP Conf. Ser. 534, Protostars and Planets VII, ed. S. Inutsuka et al. (San Francisco, CA: ASP), 233
Polychroni, D., Schisano, E., Elia, D., et al. 2013, ApJL, 777, L33
Rathborne, J. M., Jackson, J. M., Chambers, E. T., et al. 2010, ApJ, 715, 310
Reid, M. J., Dame, T. M., Menten, K. M., & Brunthaler, A. 2016, ApJ, 823, 77
Reid, M. J., Menten, K. M., Brunthaler, A., et al. 2019, ApJ, 885, 131
Ren, Z., Zhu, L., Shi, H., et al. 2021, MNRAS, 505, 5183
Rigby, A. J., Peretto, N., Adam, R., et al. 2021, MNRAS, 502, 4576
Rosolowsky, E. W., Pineda, J. E., Kauffmann, J., & Goodman, A. A. 2008, ApJ, 679, 1338
Roy, A., Martin, P. G., Polychroni, D., et al. 2013, ApJ, 763, 55
Saha, A., Tej, A., Liu, H.-L., et al. 2022, MNRAS, 516, 1983
Sánchez-Monge, A. ´, Palau, A., Fontani, F., et al. 2013, MNRAS, 432, 3288
Sanhueza, P., Girart, J. M., Padovani, M., et al. 2021, ApJL, 915, L10
Sanhueza, P., Jackson, J. M., Foster, J. B., et al. 2012, ApJ, 756, 60
Sanhueza, P., Jackson, J. M., Zhang, Q., et al. 2017, ApJ, 841, 97
Schisano, E., Molinari, S., Elia, D., et al. 2020, MNRAS, 492, 5420
Schneider, N., Csengeri, T., Hennemann, M., et al. 2012, A&A, 540, L11
Schuller, F., Menten, K. M., Contreras, Y., et al. 2009, A&A, 504, 415
Shimajiri, Y., André, P., Ntormousi, E., et al. 2019, A&A, 632, A83
Shirley, Y. L., Huard, T. L., Pontoppidan, K. M., et al. 2011, ApJ, 728, 143
Simon, R., Rathborne, J. M., Shah, R. Y., Jackson, J. M., & Chambers, E. T. 2006, ApJ, 653, 1325
Smith, R. J., Glover, S. C. O., Klessen, R. S., & Fuller, G. A. 2016, MNRAS, 455, 3640
Smith, R. J., Longmore, S., & Bonnell, I. 2009, MNRAS, 400, 1775
Sokolov, V., Wang, K., Pineda, J. E., et al. 2017, A&A, 606, A133

Solomon, P. M., Rivolo, A. R., Barrett, J., & Yahil, A. 1987, ApJ, 319, 730
Suri, S., Sánchez-Monge, A. ´, Schilke, P., et al. 2019, A&A, 623, A142
Tafalla, M., & Hacar, A. 2015, A&A, 574, A104
Taniguchi, K., Sanhueza, P., Olguin, F. A., et al. 2023, ApJ, 950, 57
Thompson, M. A., Hatchell, J., Walsh, A. J., MacDonald, G. H., & Millar, T. J. 2006, A&A, 453, 1003
Umemoto, T., Minamidani, T., Kuno, N., et al. 2017, PASJ, 69, 78
Urquhart, J. S., Csengeri, T., Wyrowski, F., et al. 2014a, A&A, 568, A41
Urquhart, J. S., Hoare, M. G., Lumsden, S. L., Oudmaijer, R. D., & Moore, T. J. T. 2008, in ASP Conf. Ser. 387, Massive Star Formation: Observations Confront Theory, ed. H. Beuther, H. Linz, & T. Henning (San Francisco, CA: ASP), 381
Urquhart, J. S., König, C., Giannetti, A., et al. 2018, MNRAS, 473, 1059
Urquhart, J. S., Moore, T. J. T., Csengeri, T., et al. 2014b, MNRAS, 443, 1555
Urquhart, J. S., Morgan, L. K., Figura, C. C., et al. 2011, MNRAS, 418, 1689
Vázquez-Semadeni, E., Palau, A., Ballesteros-Paredes, J., Gómez, G. C., & Zamora-Avilés, M. 2019, MNRAS, 490, 3061
Wang, K., Testi, L., Burkert, A., et al. 2016, ApJS, 226, 9
Webb, K. A., Di Francesco, J., Sadavoy, S., et al. 2017, ApJ, 849, 13
Wienen, M., Wyrowski, F., Schuller, F., et al. 2012, A&A, 544, A146
Xie, J., Fuller, G. A., Li, D., et al. 2021, SCPMA, 64, 279511
Xu, F., Wang, K., Liu, T., et al. 2024, ApJS, 270, 9
Xu, F.-W., Wang, K., Liu, T., et al. 2023, MNRAS, 520, 3259
Yang, A. Y., Dzib, S. A., Urquhart, J. S., et al. 2023a, A&A, 680, A92
Yang, A. Y., Thompson, M. A., Urquhart, J. S., & Tian, W. W. 2018, ApJS, 235, 3
Yang, D., Liu, H.-L., Tej, A., et al. 2023b, ApJ, 953, 40
Yuan, J., Li, J.-Z., Wu, Y., et al. 2018, ApJ, 852, 12
Zavagno, A., Dupé, F. X., Bensaid, S., et al. 2023, A&A, 669, A120
Zhang, C., Zhang, G.-Y., Li, J.-Z., & Yuan, J.-H. 2023, ApJS, 264, 24
Zhou, J.-W., Liu, T., Evans, N. J., et al. 2022, MNRAS, 514, 6038
Zinnecker, H., & Yorke, H. W. 2007, ARA&A, 45, 481